Materials Advances

PAPER

Check for updates

Hybrid silver–iron oxide nanoflowers: morphological tailoring, application as CT agents, and exploitation of induced apoptosis in glioblastoma treatment†

Sofia G. Nikolopoulou,[ab] Beata Kalska-Szostko,[c] Anna Basa,[c]
Giorgos Papanastasiou, [de] Adriana Tavares,[f] Carlos Alcaide Corral, [f]
Athina Papadopoulou, [ab] Marios Kostakis, [g] Nikolaos S. Thomaidis [g] and
Eleni K. Efthimiadou *[ab]

The ability of cancer to develop drug-resistance, in parallel with the undesired effects of chemotherapy, has led to the development of safe nanoparticles characterized by multi-sensitivity. Herein we focus on the synthesis and exploitation of the synthetic route of hybrid silver–iron oxide Nfs and their successful coating with citrate. The parameters of the synthetic route affecting the uniform formation of the Nfs are investigated to optimize the experimental route and the attained Nfs. Most importantly, the study focuses on the evaluation of the Nfs as theranostic agents in the case of glioblastoma. The results suggest that the Nfs are good candidates for CT contrast agents, as the contrast is enhanced after treatment. The *in vitro* evaluation shows that the Nfs exhibit cytotoxicity towards glioblastoma cells, whereas no significant toxicity towards red blood cells is reported. Finally, internalization studies provide insight information that helps unveil the exact mechanism of action of the Nfs.

1. Introduction

Glioblastoma (GBM) is the most common and aggressive malignant brain tumor, with an incidence of 3–5 cases per 100 000 people annually and a poor prognosis, as the median survival is only 12–18 months.[1] Current treatment options, including surgery, radiotherapy, and chemotherapy, face significant limitations. GBM's high invasiveness makes complete surgical removal difficult, while the blood–brain barrier (BBB) restricts drug delivery. Additionally, tumor heterogeneity, therapeutic resistance, immune evasion, and rapid recurrence contribute to treatment failure. Future strategies, such as nanotechnology-based drug delivery, targeted molecular therapies, immunotherapy, and gene therapies, hold promise for improving patient outcomes.[2] However, overcoming these challenges remains a major hurdle in GBM treatment. The current "gold standard" treatment combines chemotherapy, radiotherapy, and surgical interventions. Among chemotherapeutic agents, temozolomide remains the most widely used and effective, having been approved by the EMA and FDA in 1999.[3] While this multimodal approach may extend patient life expectancy, it does not achieve a complete cure or long-term survival. Consequently, extensive research has been conducted to identify vulnerabilities in glioblastoma that could lead to the development of more effective therapies.[4] In recent years, nanotechnology has emerged as a promising avenue for developing novel therapeutic agents aimed at reducing the chemotherapy side effects and overcoming cancer's drug resistance mechanisms. An increasing number of pharmaceutical products incorporate nanoparticles, underscoring their potential in cancer treatment[5–7] Multifunctional nanostructures have gained significant attention in biomedical applications, particularly for cancer therapy. Ebrahimi *et al.* (2016) synthesized, characterized, and tested silver–iron nanoparticles for apoptosis induction using flow cytometry, while their influence on bax gene expression was analyzed *via* qRT-PCR. Nanoparticles demonstrated cytotoxicity

[a] A Inorganic Chemistry Laboratory, Chemistry Department, National and Kapodistrian University of Athens, Panepistimiopolis, Zografou 157 71, Greece. E-mail: efthim@chem.uoa.gr

[b] Sol-Gel Lab, Institute of Nanoscience and Nanotechnology, NCSR "Demokritos", 153 41 Aghia Paraskevi Attikis, Greece

[c] University of Bialystok, Faculty of Chemistry, Bialystok 15-245, Poland

[d] Archimedes Unit, Athena Research Centre, Marousi, 15125, Greece

[e] School of Computer Science and Electronic Engineering, University of Essex, Colchester Campus, CO4 3SQ, UK

[f] Edinburgh Imaging Queen's Medical Research Institute, University of Edinburgh, Edinburgh EH16 4TJ, UK

[g] Laboratory of Analytical Chemistry, Department of Chemistry, National and Kapodistrian University of Athens, University Campus, Zografou, 15771, Athens, Greece

† Electronic supplementary information (ESI) available. See DOI: https://doi.org/10.1039/d5ma00210a

and apoptosis, with the strongest effect observed in the nanoparticle synthesized using glucose as a reducing agent. Upregulation of bax gene expression suggested activation of the intrinsic apoptosis pathway, influenced by stress-related transcription regulators. These findings highlight the potential of silver–iron oxide hybrid nanoparticles for targeted cancer therapy by taking into advantage their dual nature.[8] Iron oxide nanoparticles have emerged as promising agents for cancer diagnosis and treatment due to their magnetic properties and biocompatibility. These nanoparticles can be functionalized with drugs or phytochemicals for targeted delivery and have applications in thermoablation, hyperthermia, and magnetic resonance imaging (MRI).[9] Das *et al.* (2016) report that Ag/Fe_3O_4 nanoflowers boost the specific absorption rate by one order of magnitude under combined magnetic and laser irradiation.[10] Erdogan *et al.* (2021) demonstrate that silver nanoparticles produced *via* green chemistry reduce cell proliferation and migration in U87 glioblastoma cells, a change accompanied by lower Bcl-2 levels and higher Bax and caspase-3 activities.[11] Gholami *et al.* (2018) describe chitosan nanoparticles loaded with doxorubicin that deliver the drug in a pH-sensitive manner and shorten T_2 relaxation times in C6 glioma cells. Nikolopoulou *et al.* (2023) notes that hybrid Ag@SiO_2 core–shell nanoparticles exert anticancer effects against glioblastoma cells while exhibiting only minor toxicity toward healthy cells,[12] and Zhang *et al.* (2021) indicates that metal–phenolic network nanoparticles elevate intracellular reactive oxygen species and induce ferroptosis, along with enhanced MRI and photothermal responses.[13] Reported particle sizes span approximately 141 to 184 nm, while synthesis methods range from green chemistry and ionic gelation to modified sol–gel techniques. Reaction time and the Ag/Fe ratio prove to influence nanoparticle morphology and dual imaging capability *via* silver or iron components. These findings support the view that silver-based and hybrid silver–iron nanoparticles can serve as multifunctional agents in glioblastoma theranostics. Other studies have explored combining iron oxide nanoparticles with other materials to enhance their functionality. Conjugated polymer nanoparticles incorporating iron oxide cores have been developed for simultaneous MRI and fluorescent imaging of brain tumors.[14] Similarly, silver/iron oxide hybrid nano-popcorns have shown potential for imaging and therapy, demonstrating photothermal thrombolytic effects, anticancer activity, and MRI capabilities. These hybrid nanoparticles exhibited low toxicity and no long-term retention in mouse organs, suggesting their potential for diagnosing and treating various diseases.[15] Generally, an approach for multi-sensitive nanomaterials has been recently reported in literature, where iron is contributing to the diagnostic potential of the nanomaterials, whilst the incorporation of noble metals such as silver improves the response to phototherapy.[16]

Based on the recent silver–iron nanoparticles studies, our work investigates the theranostic potential of hybrid Nfs, focusing on understanding the mechanisms underlying their formation during synthesis. Key synthesis parameters are examined to determine the optimal conditions for producing Nfs with desirable properties. The physicochemical characteristics of the Nfs are analyzed using various techniques, including size measurement methods, FT-IR, UV-Vis spectroscopy, and pXRD. Additionally, the theranostic potential of the Nfs is evaluated through *in vitro* protocols, including cytotoxicity assays, internalization studies, reactive oxygen species (ROS) evaluation, and hemocompatibility tests. These biological assessments provide insights into the Nfs' biocompatibility, ability to induce oxidative stress, and cellular localization, as observed *via* microscopy techniques. Additionally, the theranostic potential of the Nfs is evaluated through *in vitro* protocols, including cytotoxicity assays, internalization studies, reactive oxygen species (ROS) evaluation, and hemocompatibility tests. These biological assessments provide insights into the Nfs' biocompatibility, ability to induce oxidative stress, and cellular localization, as observed *via* microscopy techniques.

The results indicate that uniform Nfs form under extended reaction times and low Ag/Fe ratios. Longer reaction times are associated with increased Nf size, while citrate coating has minimal impact on their physical properties. *In vitro* studies suggest that both coated and uncoated Nfs exhibit anticancer activity while maintaining hemocompatibility. Their fluorescence (due to silver content) and detectability through iron-based Prussian blue staining highlight their dual diagnostic and therapeutic capabilities.

The CT measurements along with apoptosis–necrosis evaluation and identification of endocytosis pathway verify the possible anticancer activity of the Nfs as well as their potential use as contrast agents in diagnostic techniques such as CT scan. In contrast to previously published studies, this research provides novel insights into the coating process of these nanoflowers (Nfs) and its impact on their biological activity, which, to the best of our knowledge, has not been previously reported. To date, biological applications of such Nfs are scarcely reported in the literature, underscoring the novelty and importance of this study. To our knowledge, this is the first investigation into their potential for glioblastoma diagnosis and treatment, paving the way for further research in this field.

It is also noteworthy that these exotic morphologies are rarely encountered in the literature, and increased documentation can significantly enhance the overall understanding of this category of materials.

2. Results and discussion

2.1 Synthesis of silver–iron oxide Nfs (SIONFs)

Hybrid SIONFs are synthesized *via* a solvothermal process, wherein silver (forming the core of the Nf) is reduced first, followed by the reduction of iron to create petal-like structures around the silver core. These complex nanoarchitectures of silver and iron oxide are not well-documented in the literature, with only a few studies published to date. Building on, previous work, such as Zhang *et al.* (2012), which explored the formation mechanism of Nfs with varying Ag/Fe ratios and reaction times,[7] this study further investigates the effects of these synthetic parameters. Specifically, we evaluated Ag/Fe ratios of 0.15, 0.18, and 0.20, alongside reaction times of 6, 8, 12, and 24 hours, to determine their impact on the size, morphology, and structure of the Nfs. (Table 1). Since there is only one

Table 1 Synthetic parameters for different Nfs and TEM size values

Nfs	Ag/Fe ratio	Reaction time	TEM size of Nfs
Nf 24H 0.2R	0.2	24 h	80.75 nm ± 10.12
Nf 8H 0.15R	0.15	8 h	54.36 nm ± 13.40
Nf 6H 0.18R	0.18	6 h	47.42 nm ± 12.87
Nf 12H 0.2R	0.2	12 h	83.25 nm ± 15.89
Nf 12H 0.18R	0.18	12 h	68.00 nm ± 13.28

Table 2 Comparison of our tested parameters with literature available data

Case study	Ag/Fe ratio	Reaction time
Current study	0.2	24 h
	0.15	8 h
	0.18	6 h
	0.2	12 h
	0.18	12 h
Literature available data	0.15	4 h
	0.30	8 h
	0.60	8 h

reference in literature so far concerning these parameters, we obtain results with different ratios of precursors and reaction times and are able to confirm the proposed conclusions regarding the effect of the synthetic parameters on the result of the size and shape of the obtained nanoparticles and support it with additional data (Table 2).[17] From the TEM results as far as morphology is concerned, we notice that the increase of the reaction time leads to formation of uniform Nfs with district cores and petals. On the other hand, when comparing the results with the different ratios of silver and iron the changes in shape are not so obvious. While increasing the ratio of silver : iron there is a slight increase on the size of the Nfs, while the Nfs shape is more uniform (Fig. 1).

2.2 Physicochemical characterization

The colloidal stability of the Nfs is studied by DLS and Zeta potential measurements. The determination of size by the DLS can be different from the results of TEM, because DLS calculates the hydrodynamic diameter of the nanoparticles and not their actual size. These differences in size can be attributed to the fact that the nanoparticles exhibit intramolecular interactions with the dispersant, herein is water, that can cause an increase in the measured size by DLS[18] (Table 3 and Fig. 2, Fig. S1–S3, ESI†). The structural characterization of the Nfs includes the UV-Vis study, the FT-IR and PXRD spectra of the synthesized Nfs. The hybrid nature of the Nfs results in two absorbance peaks in the UV-Vis study, which are accredited to silver and iron. Silver is known to appear SPR band at the UV-Vis region at around 00 nm.[19,20] As shown in the obtained spectra, the presence of silver is confirmed by the appearance of these absorbance bands in all the synthesized Nfs. The shifting of the silver peak from one case to another is caused by the different sizes of the silver cores formed. A shift to the red region complies with an increase in the size of the silver core. In a similar way the shifting in the iron's peak at around 700 nm can be explained (Fig. 2).[17] In the FT-IR spectra of the Nfs characteristic carboxyl group C=O, C–O stretching and
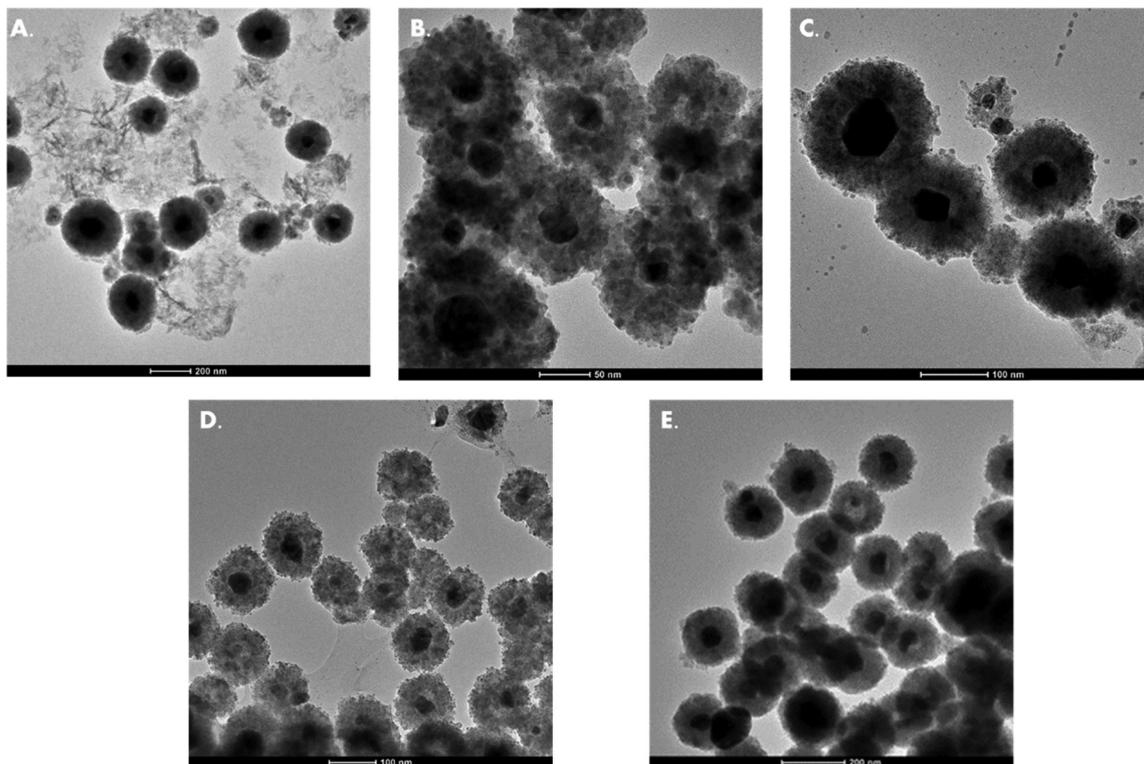

Fig. 1 TEM images of (A) Nf 24H 0.2R, (B) Nf 8H 0.15R, (C) Nf 6H 0.18R, (D) Nf 12H 0.2R and (E) Nf 12H 0.18R.

Table 3 Results of DLS, zeta potential and TEM of synthesized Nfs

Nfs	d_{DLS} (nm)	ζ (mV)	PdI index	$d_{TEM size}$ (nm)
Nf 24H 0.2R	220.3	−21.4	0.300	80.8
Nf 8H 0.15R	971.4	−16.1	0.359	54.4
Nf 6H 0.18R	1078	−2.82	0.444	47.4
Nf 12H 0.2R	296	−14.3	0.374	83.2
Nf 12H 0.18R	396.3	−14.8	0.289	68

O–H stretching attributed to the sodium acetate stabilizing the Nfs is detected at 1634 cm^{-1}, 1038 cm^{-1} and 3263 cm^{-1} respectively (Fig. 3), confirming the role of sodium acetate as a stabilizing agent.[21]

Powder X-ray diffraction (pXRD) is a key characterization method for determining the properties of nanoparticles. XRD measurements provide valuable insights into crystal structures, which can be crucial for evaluating their potential applications, such as use as contrast agents. In this study, the characteristic XRD peaks observed in all cases of the Nfs indicate that iron is present as magnetite, with notable planes at (220), (311), (400), (511), and (440). This finding aligns with the experimental observation of the Nfs' magnetization during the washing process at the conclusion of the synthesis (Fig. 4). For silver, the characteristic planes observed at (111), (220), and (200) correspond to a face-centered cubic (fcc) structure, confirming the crystallinity of the Nfs.[22]
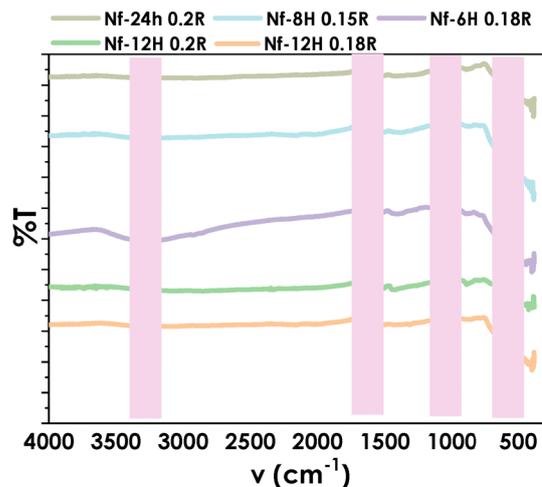

Fig. 3 FT-IR spectra of the Nfs.

2.3 Coating of Nfs with citrate

2.3.1 Physicochemical characterization of coated Nfs. To improve Nfs colloidal stability as well as their biocompatibility Nfs are divided into three basic groups and are functionalized with citrate. The Nfs are physicochemically and biologically characterized to study the impact of the coating on and the corresponding properties. The coating is successfully completed by mixing the
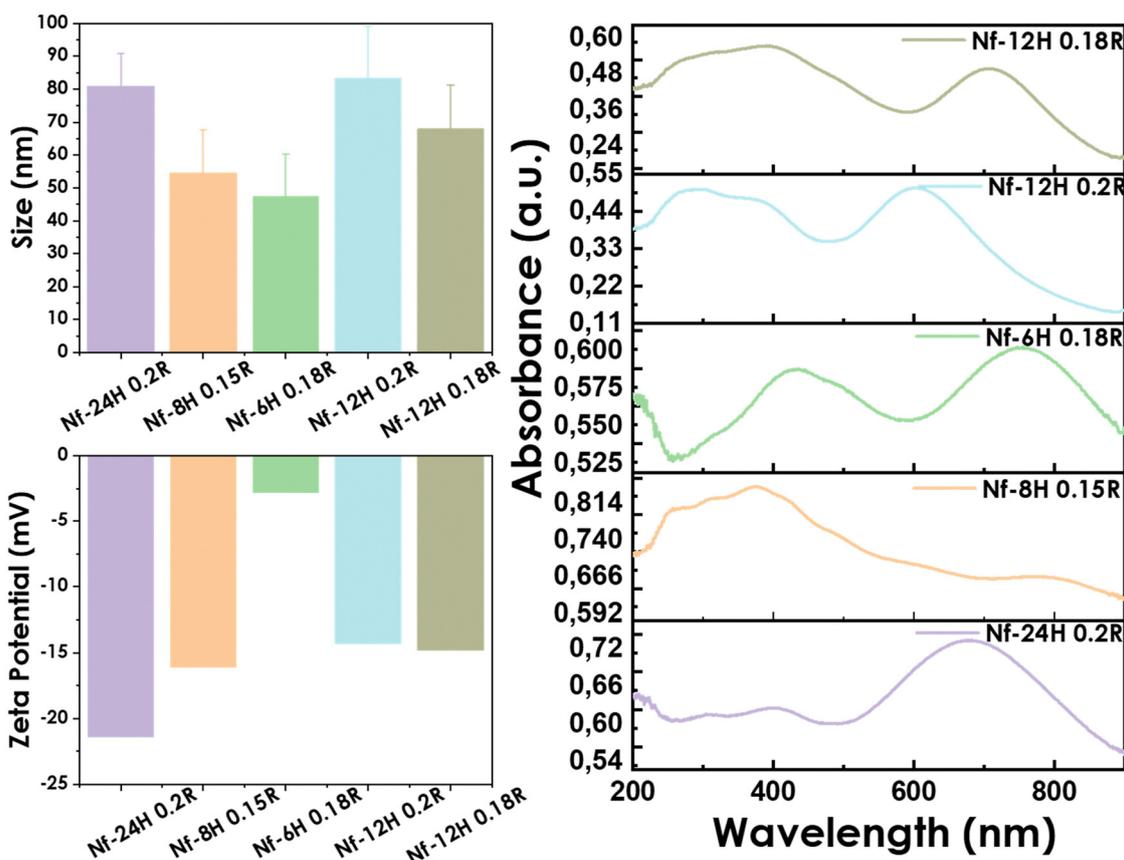

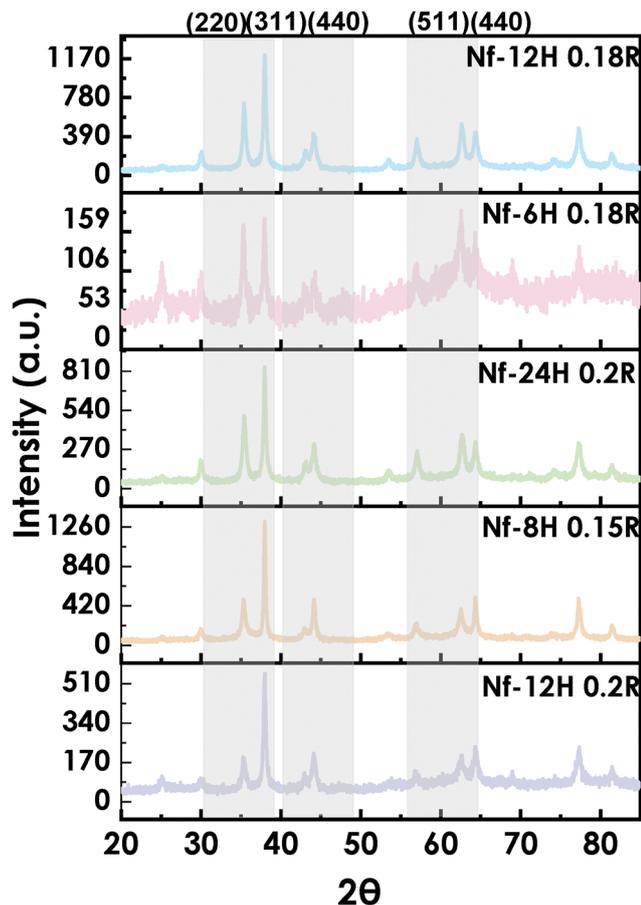**Fig. 2** Size (TEM), zeta potential and UV spectra of the hybrid Nfs.

Fig. 4 Comparative pXRD spectrums of hybrid Nfs.

Fig. 6 UV-Vis spectra of coated-coated Nfs.

obtained Nfs that were dispersed in water with trisodium citrate and leaving the admixture under stirring at a speed of 1200 ppm and at 60 °C overnight. Specifically, in a spherical flask of 10 mL, 5 mL of uncoated nanoflowers were added followed by the addition of trisodium citrate to achieve a final concentration of 1 mg mL^{-1}, which is considered an adequate quantity to achieve the coating of the nanoflowers due to the absence of a coating of increased stability. The purification of the Nfs is followed by multiple washings with ethanol (x2) and water (x3) using a magnet, in order to remove excess unreacted citrate. The resulting coated Nfs are redispersed in water for further characterization. The morphology as expected did not show any changes from the coating process (Fig. 5). The primary physicochemical characterization of the coated Nfs includes DLS and TEM measurements and the studies of the UV-Vis and IR spectrums.

As shown in Fig. 6, the peaks of silver and iron do not change significantly, indicating the stability of the Nfs after the coating process and the maintenance of these specific physicochemical properties.

The DLS results show the improvement of colloidal stability, which translates to lower PdI values and negatively higher Zeta Potential values (Table 4 and Fig. S4, S5, ESI†). As elaborated
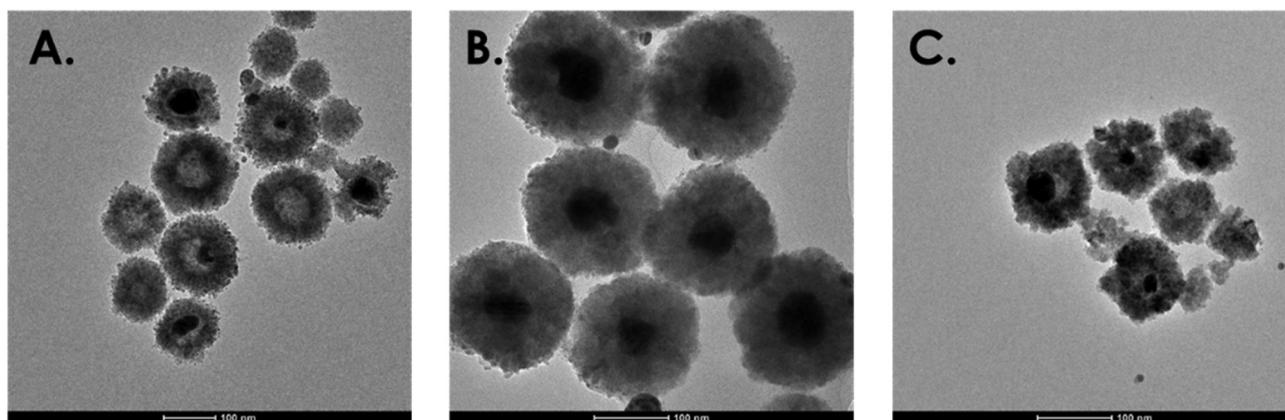

Fig. 5 TEM images of citrate-coated Nfs (A) Nf 6H 0.18R, (B) Nf 12H 0.2R, (C) Nf 12H 0.18R.

Paper

Materials Advances

Table 4 Results of DLS, zeta potential and TEM of citrate-coated Nfs

Nanoflowers	$d_{H(DLS)}$ (nm)	ζ (mV)	PdI index	d_{TEM} (nm)
Nf@citrate 12H 0.18R	147.0	−18.8	0.156	98.6
Nf@citrate 12H 0.2R	246.4	−19.1	0.236	52.4
Nf@citrate 6H 0.18R	190.4	−17.8	0.293	107.3

widely in literature, low PdI values are associated with increased uniformity of the obtained nanoparticles, which is crucial for the subsequent biological applications.[23,24] Moreover, the FT-IR spectra of the coated Nfs (Fig. 7) confirms the presence of the coating, due to the stretching vibrations observed at 1350 cm^{-1} and 1600 cm^{-1}, attributed to the stabilizing molecules of citrate.

2.3.2 Computed tomography imaging. CT imaging was used to measure the contrast-enhancing properties of both, the bare silver Nfs and citrate-coated silver Nfs. We investigated four different silver concentrations (0.001, 0.01, 0.02, and 0.05 mM) to determine if a concentration-dependent CT signal enhancement could be observed. CT signal intensity increased with rising silver concentration in both types of nanoparticles (Fig. 8(A) and (B)). No significant difference in CT signal was observed between the bare and citrate-coated silver Nfs at corresponding concentrations, suggesting that the citrate coating does not substantially impact the contrast enhancement efficacy. It is worth noting that the quantitative analysis of CT signal (Fig. 8(A) and (B)) revealed consistent trends, while subtle
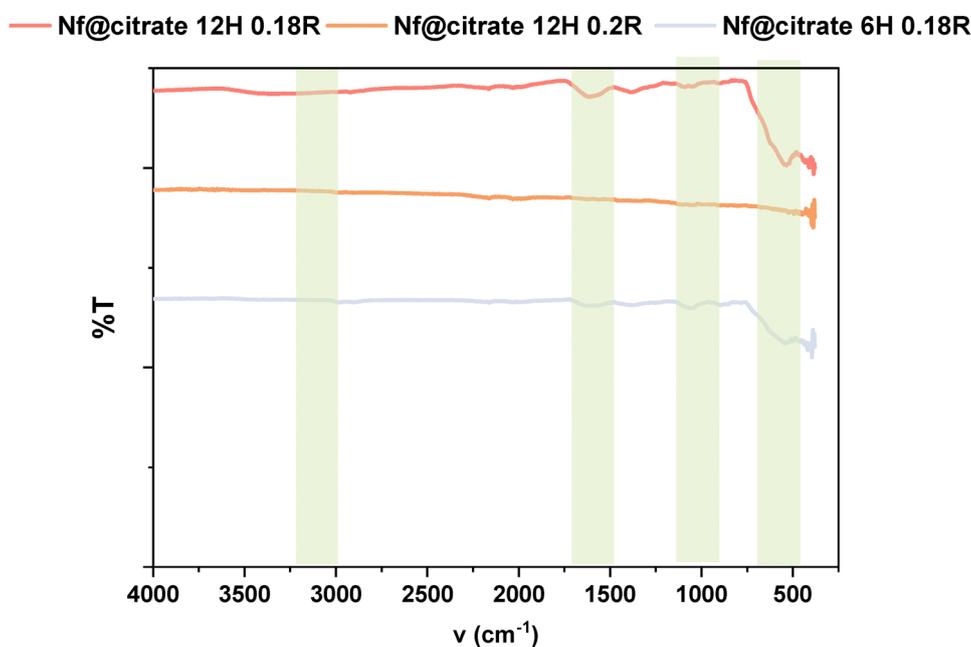

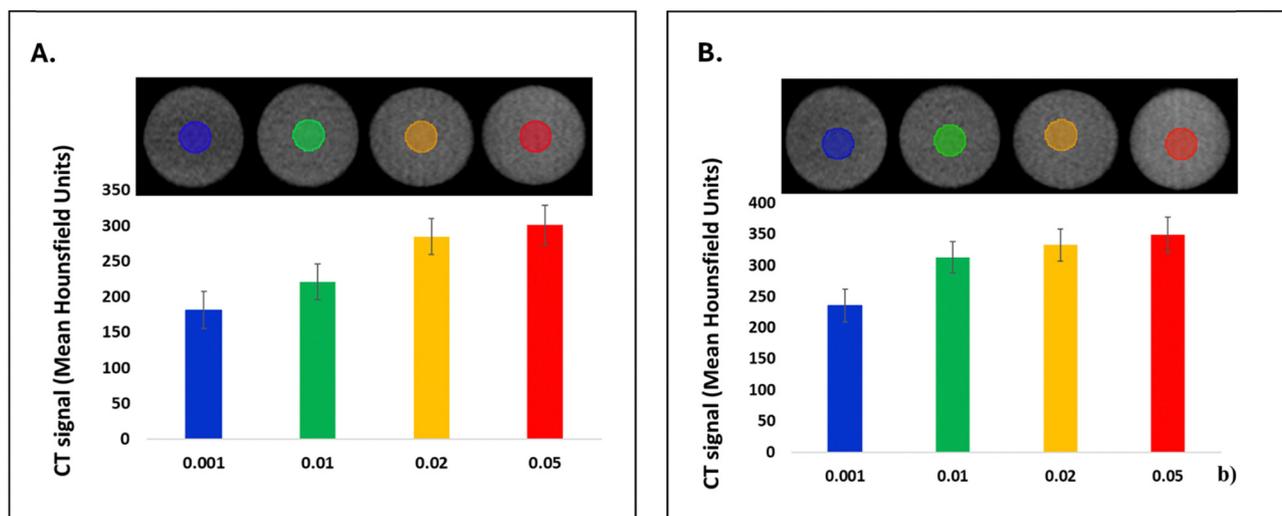**Fig. 7** FT-IR spectra of the citrate-coated Nfs.

Fig. 8 Computed tomography imaging and analysis of the Nfs (a) and the citrate-coated Nfs (b).

differences were sometimes difficult to discern visually. It is of outmost important to emphasize that there exists only one other literature reference regarding the diagnostic potential of the hybrid silver–iron oxide nanoflowers. However, the findings of Wang *et al.* suggest that the nanoflowers are suitable for MRI agents, whereas the present study investigates and demonstrates the application of the nanoflowers as CT agents. Nevertheless, both studies corroborate and support the presence of dual properties in the nanoflowers and thus their multipurpose nature.[25] Lastly, it is important to highlight the findings of Moonshi *et al.* that proved the effectiveness of iron–silver nanospikes as dual-imaging tools.[26]

2.4 Biological evaluation of hybrid Nfs and coated hybrid Nfs

2.4.1 Hemocompatibility study. Both coated and uncoated hybrid Nfs exhibit negligible to no hemolysis (Fig. 9), indicating their hemocompatibility, a critical factor for theranostic applications. These findings are further supported by the optical examination of the supernatants after centrifugation, where the absence of a red color confirms the lack of released hemoglobin.[27,28] (Fig. S8, ESI†).

While hemolysis results provide insights into toxicity toward red blood cells (RBCs), they may not reveal indirect toxicity, such as structural abnormalities, which can ultimately lead to cell death. However, as shown in Fig. 10(a)–(c), no structural alterations were observed for any of the tested Nfs, supporting their presumed high biocompatibility with RBCs.[29]

2.4.2 *In vitro* cytotoxicity study. Both bare and coated Nfs are evaluated in both healthy (HaCat) (Fig. 11(a) and (b)) and cancer cells (U87-MG) (Fig. 12(a) and (b)) to exploit their anticancer properties. The results of the MTT assay indicate a concentration-dependent effect on cell viability in both healthy and cancer cell lines. Notably, the coating plays a significant role in determining the resulting toxicity. The highly negative surface potential of the coated Nfs enhances their interaction

with cell membranes, leading to increased toxicity. While this may seem contradictory to the protective intent of a coating, similar effects have been reported in the literature and could explain the preference for alternative coating materials, such as PEG or polysaccharides. The purpose of using citrate as a coating agent was to specifically investigate its effects and draw conclusions, as no prior data exists for Nfs with this type of coating.[30,31] Additionally, it is well-established that nanoparticle size is inversely proportional to cell viability, further contextualizing the observed effects.[32] The present study does not identify such a pattern, which can be attributed to the "exotic" morphology of the Nfs and the resulting complexity of their exact mechanism of toxicity toward cells. An extensive literature review has been conducted to further substantiate the obtained data. It is widely documented that citrate is among the most prevalent coating materials. Two principal factors have been identified to account for the increased toxicity of the coated nanoflowers. Firstly, the enhanced negative surface charge on the nanoparticles' surface leads to their aggregation, thereby increasing toxicity. Secondly, a recent study demonstrated that greater coating complexity results in reduced oxidation, thereby decreasing the toxicity of the coated nanomaterials. Given that citrate is not considered complex as a coating material and based on the previously mentioned data, this finding supports and elucidates the obtained data.[33,34]

Regarding the statistical analysis that is performed for the cytotoxicity results obtained, it should be noted that One-way Anova is considered an appropriate statistical tool that is suitable for the analysis of the difference (if occurs) between the mean values of two or more groups. It is important to analyze and conclude the difference between the different nanoflowers and different concentrations, as those conclusions can lead to in depth understanding and linkage of the nanoparticle's toxicity with respects to their properties. Also, it should be noted that the
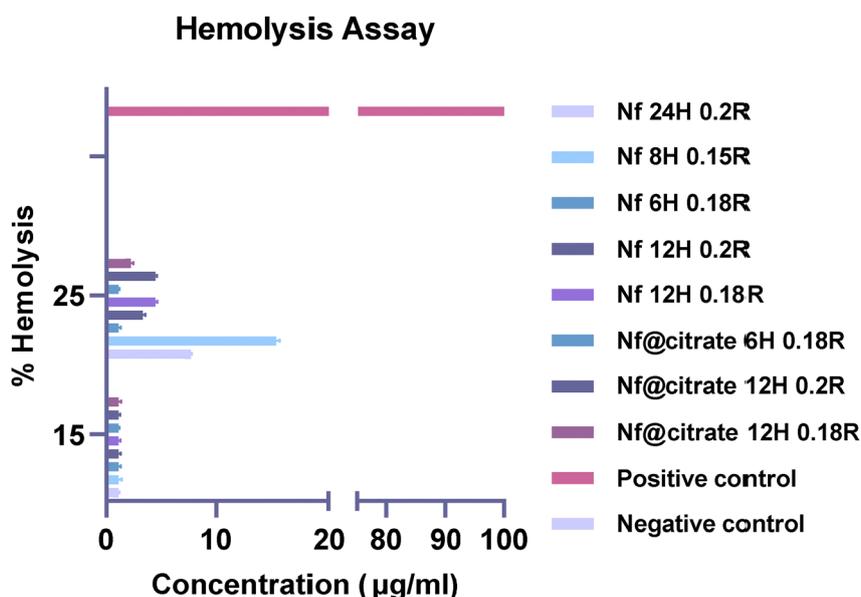

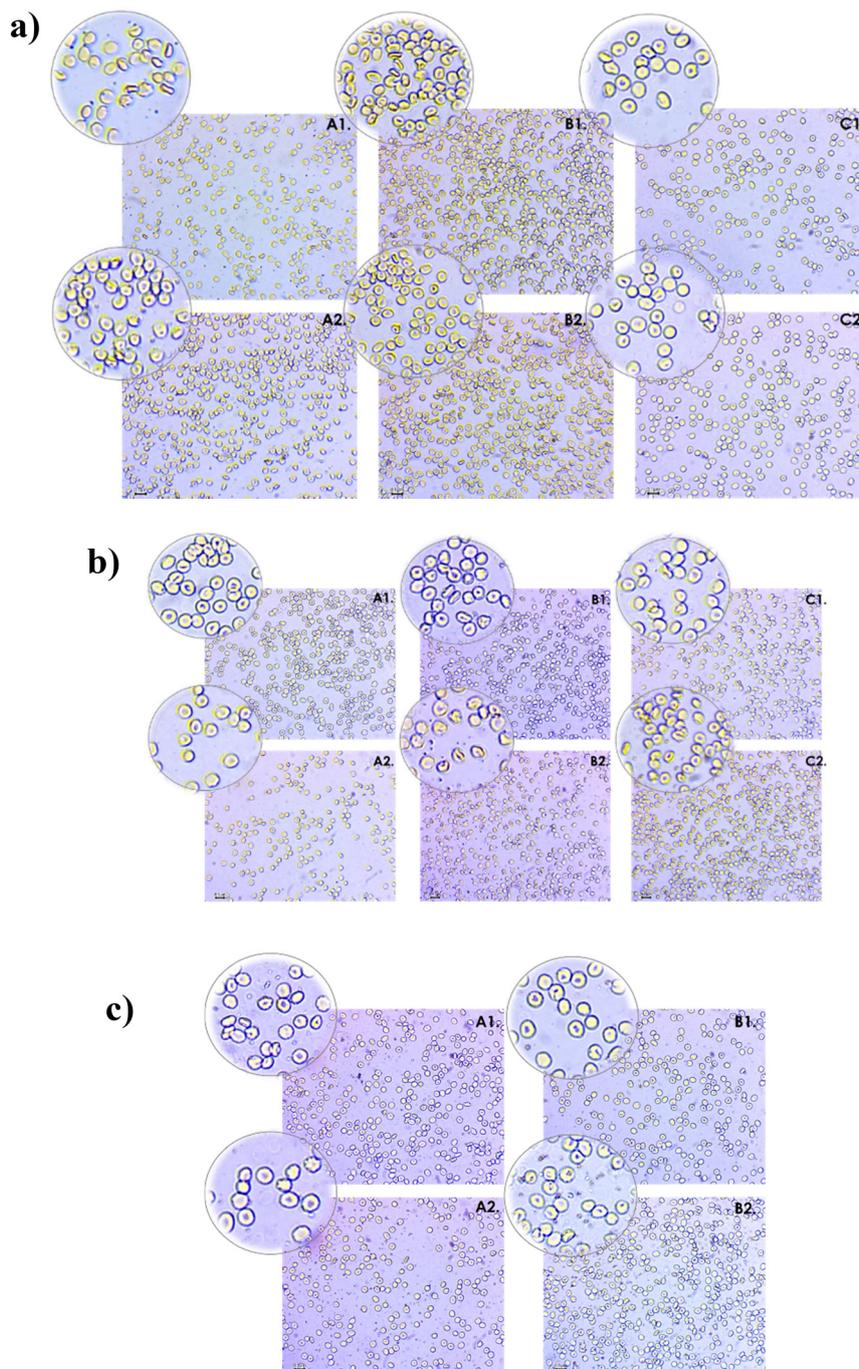**Fig. 9** % Hemolysis of RBCs after 3 h treatment with synthesized NPs.

Fig. 10 (a) Optical observation of RBCs after incubation with (A1), (A2) Nf 24H 0.2R, (B1), (B2) Nf 8H 0.15R and (C1), (C2) Nf 6H 0.18R, at concentrations 1: 15 μg mL^{-1} and 2: 25 μg mL^{-1}. (b) Optical observation of RBCs after incubation with (A1), (A2) Nf 12H 0.2R, (B1), (B2) Nf 12H 0.18R, at concentrations 1: 15 μg mL^{-1} and 2: 25 μg mL^{-1}. (c) Optical observation of RBCs after incubation with (A1), (A2) Nf@citrate 6H 0.15R, (B1), (B2) Nf@citrate 12H 0.2R and (C1), (C2) Nf@citrate 12H 0.18R, at concentrations 1: 15 μg mL^{-1} and 2: 25 μg mL^{-1}.

study is repeated three times, in order to ensure the robustness of the findings, due to the high variability of the MTT assay. Moreover, the robustness of the method used has been ensured by the use of DMSO that increases the accuracy of the MTT assay, as suggested in literature.[35] At this point it is important to clarify and justify the difference that is observed between healthy and cancer cells. As mentioned in literature due to the

higher metabolic activity of tumour cells, there is higher ROS production and this leads to the susceptibility of cancer cells to present ferroptosis. On the contrary, this phenomenon does not take place in healthy cells. Given the increased iron availability inside glioblastoma cells, this explains why there is higher toxicity of the hybrid nanoflowers towards U87-MG cells than HaCat cells. The abovementioned rationale explains sufficiently
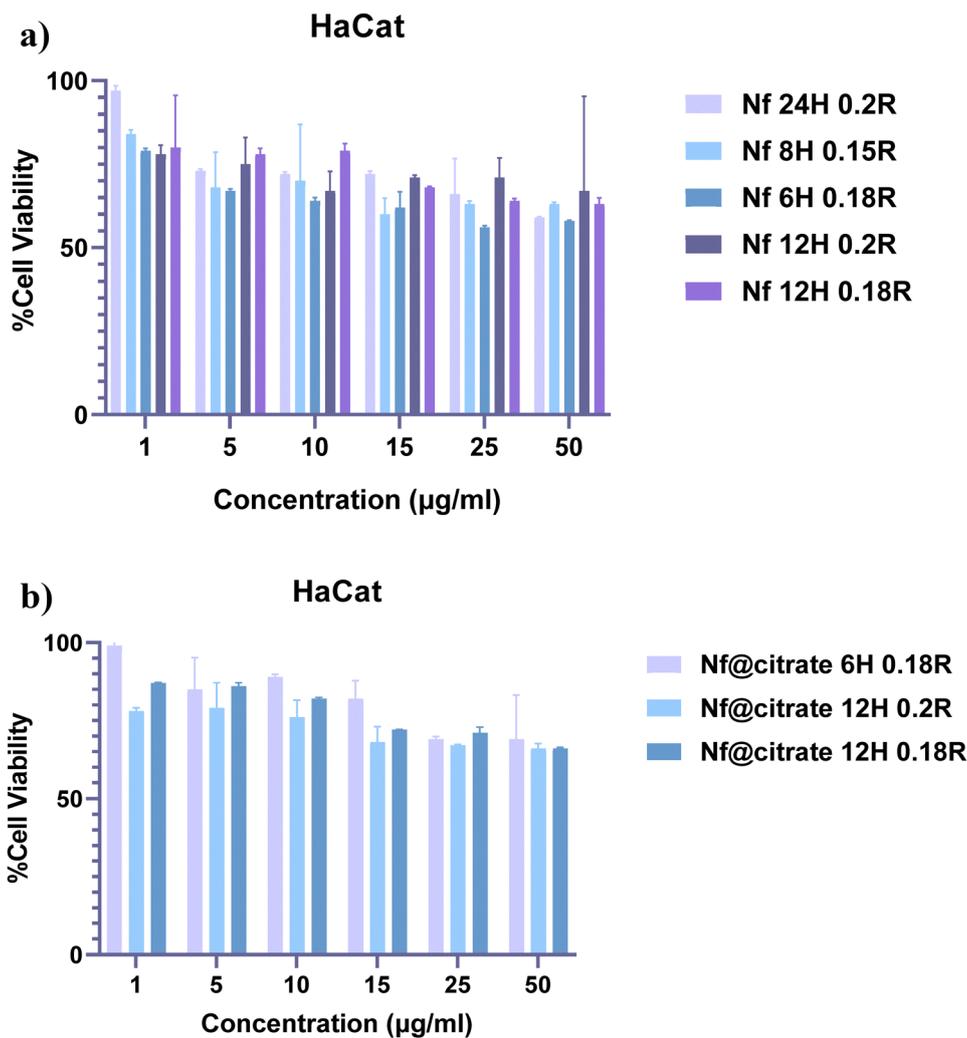
Fig. 11 (a) *In vitro* toxicity of hybrid uncoated Nfs in healthy HaCat cells. (Statistical analysis by One-way ANOVA with Tuckey multiple comparisons, ns: non-significant). (b) *In vitro* toxicity of hybrid coated Nfs in healthy HaCat cells. (Statistical analysis by One-way ANOVA with Tuckey multiple comparisons, ns: non-significant).

the difference in the results of healthy and cancer cells.[36–39] The abovementioned conclusion has been also confirmed by a recent study on iron–silver nanospikes and their effectiveness as dual imaging probes as well as synergestic chemotherapeutics.[26]

2.4.3 Internalization studies. The dual nature of the synthesized Nfs possesses several advantages on their biological properties but also facilitates their study by taking advantage of different evaluation methods based on silver or iron oxide present.

2.4.3.1 Investigation of internalization by Prussian blue protocol. The presence of iron oxide on the outer part of the Nfs enables their tracking using the Prussian blue staining protocol. Treatment with the Pearls reagent results in a blue coloration at the locations of the Nfs within the cells. This allows for confirmation of their internalization and investigation of their specific localization. In Fig. 13(a)–(c), the internalization inside healthy HaCat cells is observed. In all cases of Nfs, blue spots can be identified at the outer lining of the cells. No significant

differences can be observed, except the cases of Nf 24H 0.2R and Nf 12H 0.18R where there seems to be higher internalization and can be attributed to their smaller size.

The same procedure is followed for the study regarding glioblastoma cells. As shown in Fig. 14(a)–(c), the internalization compared to healthy cells is much more intense. These results suggest that internalization is more favorable in glioblastoma cells compared to healthy cells.[40,41] Regarding both cases (healthy and cancer cells) it is noted that the results of the staining are not in agreement with the cytotoxicity study results *e.g.* Nf 6H 0.18R. To clarify the light staining of the cells compared to the significant cytotoxicity levels, the first step is the literature review for any available data regarding this type of Nfs. Since these tests have not been reported so far, the next step is the careful examination of the protocol and the principles of the method. As it is extensively reported, the Prussian blue staining appears during the reduction of only Fe^{3+} ions by the Pearls reagent. In the present case of Nfs, the pXRD results show that the crystalline structure of all the Nfs is magnetite,
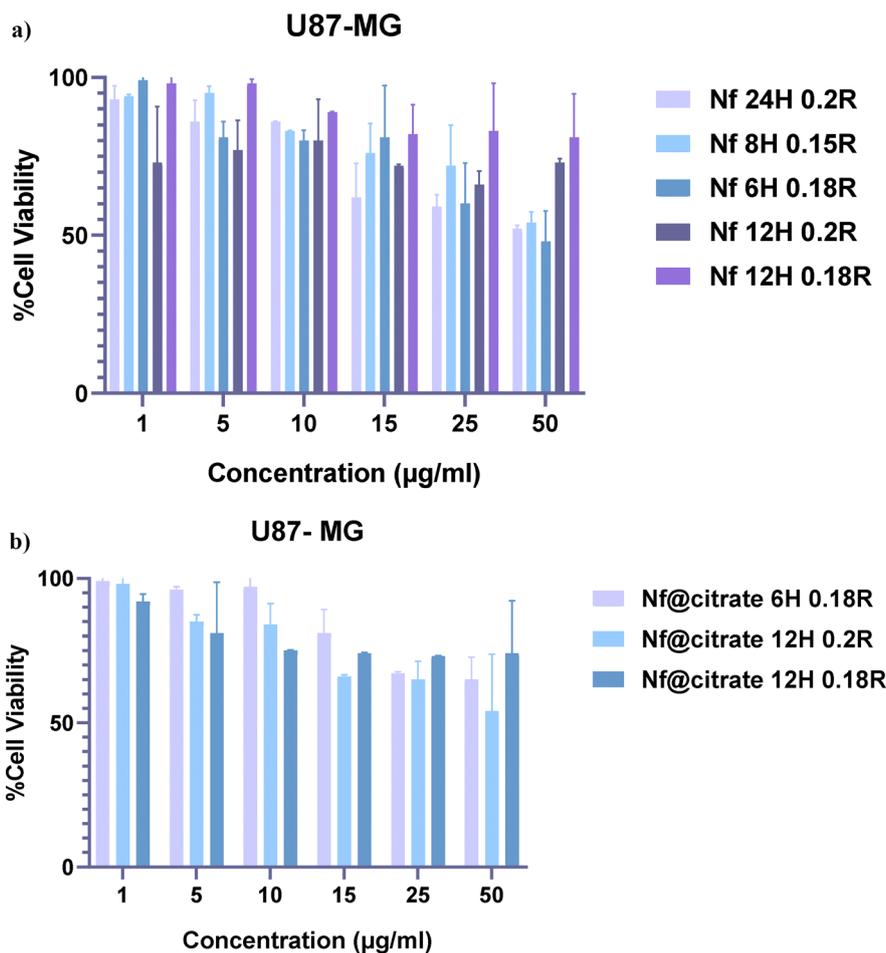
Fig. 12 (a) *In vitro* toxicity of hybrid uncoated Nfs in glioblastoma U87-MG cells. (Statistical analysis by One-way ANOVA with Tuckey multiple comparisons, ns: non-significant). (b) *In vitro* toxicity of hybrid coated Nfs in glioblastoma U87-MG cells. (Statistical analysis by One-way ANOVA with Tuckey multiple comparisons, ns: non-significan.

which is found both as Fe^{3+} and Fe^{2+}. Thus, the possible explanation behind some cases with no significant Prussian blue staining, lies in the quantitative ratio of the two oxidative states. Although, this is a logical justification of the observations, the possible explanation is confirmed by conduction of internalization studies by fluorescence microscopy.[42] Furthermore, the results of the Prussian Blue staining demonstrate a greater internalization in glioblastoma cells compared to healthy cells. This observation aligns with the rationale discussed in the cytotoxicity section and is consistent with the findings of the MTT assay. Additionally, the size distribution and morphology of the nanoflowers are correlated with the cellular uptake results, as indicated by the Prussian Blue staining. As illustrated in the microscopy images, nanoflowers with lower PDI values exhibit higher accumulation within cells, resulting in more intense blue staining. This phenomenon can be attributed to the fact that more aggregated nanoflowers encounter difficulty in entering cells, thereby reducing observable staining. The aforementioned conclusion concurs with a recent study that demonstrated the PDI of nanoparticles exerts a greater influence on their internalization than their ζ potential[39]

. Regarding the influence of shape, it is observed that more uniformly shaped nanoflowers exhibit more intense internalization. The presence of more "exotic" morphologies has been reported to cause higher internalization into cells due to an increased surface area that enhances interactions with cells. Nevertheless, given the similar shape of the nanoflowers across all synthetic procedures, no specific comparisons are applicable in the present report, as no significant differences in shape are observed.[43–45]

2.4.3.2 Investigation of internalization by fluorescence microscopy. As mentioned at the previous study, the duality of the Nfs' nature offers monitoring of their action inside the cells by different protocols based on either silver or iron. It is known that silver nanoparticles often exhibit fluorescence due to their unique optical properties.[12] The pictures of the fluorescence microscopy show intense green fluorescence of the Nfs, confirming the successful internalization of the Nfs and supporting the proposed explanation of the previous study results (Prussian blue staining). In detail, Fig. 15(a)–(c) depict the fluorescence of all Nfs coated inside healthy cells (HaCat).
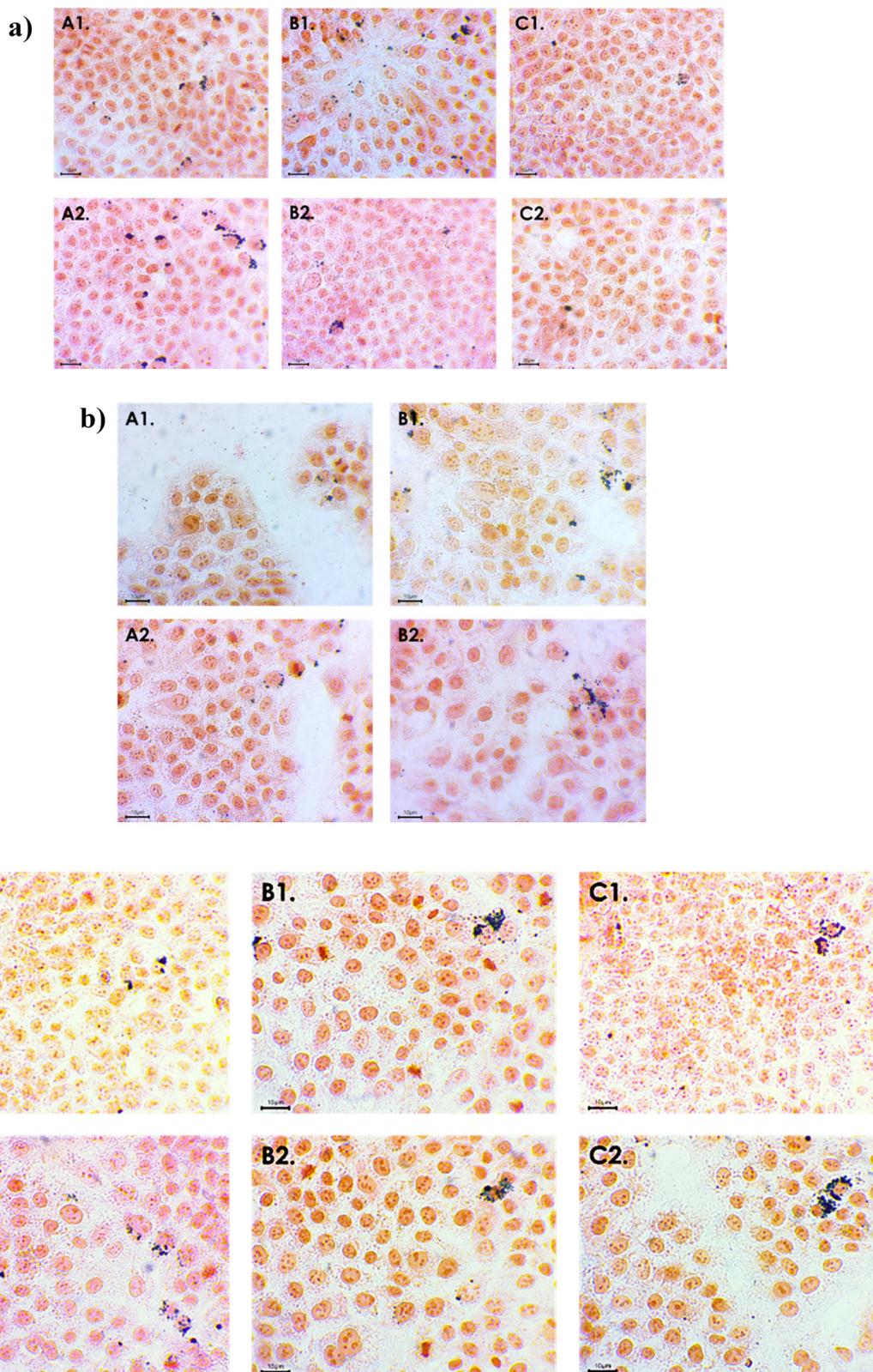
Fig. 13 (a) Optical microscopy images of HaCat cells treated with (A1–2) Nf 24H 0.2R, (B1–2) Nf 8H 0.15R and (C1–2) Nf 6H 0.18R and stained with Prussian Blue after 24 h incubation, at concentrations 1: 15 µg mL^{-1} and 2: 25 µg mL^{-1}. (Scale bar: 10 µm). (b) Optical microscopy images of HaCat cells treated with (A1–2) Nf 12H 0.2R, (B1–2) Nf 12H 0.18R and stained with Prussian Blue after 24 h incubation, at concentrations 1: 15 µg mL^{-1} and 2: 25 µg mL^{-1}, (Scale bar: 10 µm). Optical microscopy images of HaCat cells treated with (A1–2) Nf@citrate 6H 0.18R, (B1–2) Nf@citrate 12H 0.2R and (C1–2) Nf@citrate 12H 0.18R and stained with Prussian Blue after 24 h incubation, at concentrations 1: 15 µg mL^{-1} and 2: 25 µg mL^{-1}. (Scale bar: 10 µm).
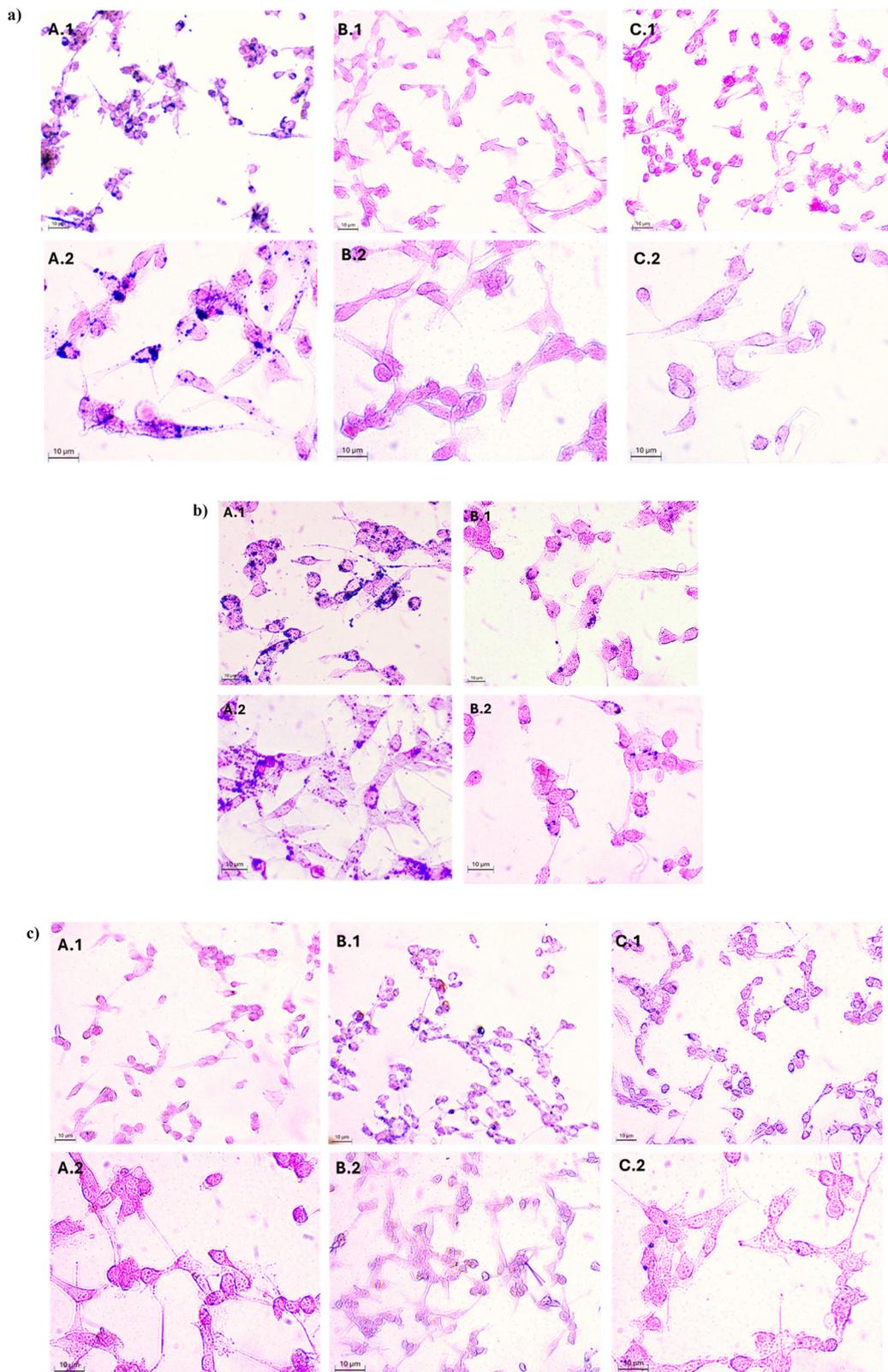
Fig. 14 (a) Optical microscopy images of U87-MG cells treated with (A1-2) Nf 24H 0.2R, (B1-2) Nf 8H 0.15R and (C1-2) Nf 6H 0.18R and stained with Prussian Blue after 24 h incubation, at concentrations 1: 15 µg mL^{-1} and 2: 25 µg mL^{-1}. (Scale bar: 10 µm). (b) Optical microscopy images of U87-MG cells treated with (A1-2) Nf 12H 0.2R, (B1-2) Nf 12H 0.18R and stained with Prussian Blue after 24 h incubation, at concentrations 1: 15 µg mL^{-1} and 2: 25 µg mL^{-1}. (Scale bar: 10 µm). (c) Optical microscopy images of U87-MG cells treated with (A1-2) Nf@citrate 6H 0.18R, (B1-2) Nf@citrate 12H 0.2R and (C1-2) Nf@citrate 12H 0.18R and stained with Prussian Blue after 24 h incubation, at concentrations 1: 15 µg mL^{-1} and 2: 25 µg mL^{-1}. (Scale bar: 10 µm).
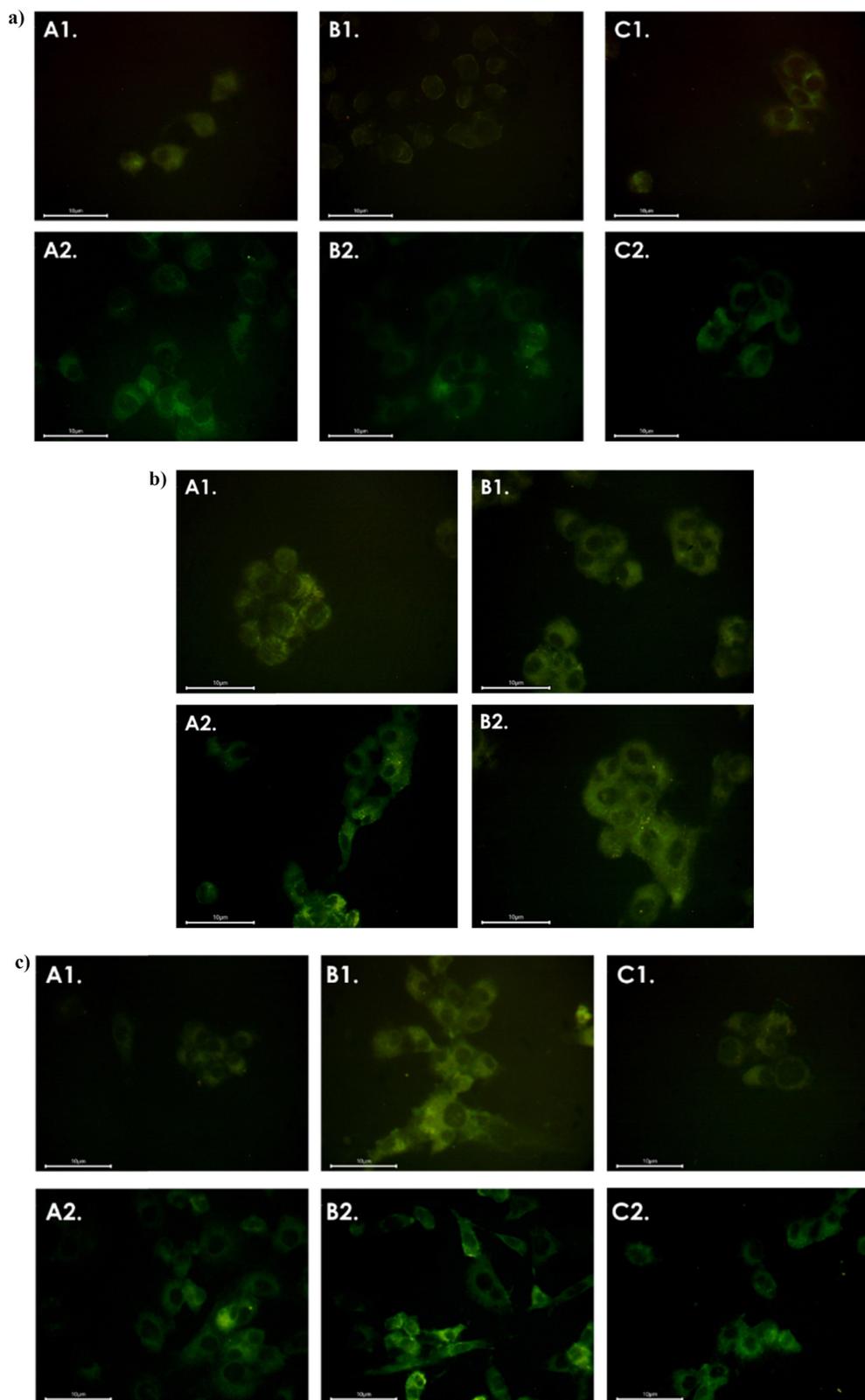
Fig. 15   (a) Fluorescence microscopy images of HaCat cells after 24 h incubation with (A1-2) Nf 24H 0.2R, (B1-2) Nf 8H 0.15R and (C1-2) Nf 6H 0.18R, at concentrations 1: 15 µg mL^{-1} and 2: 25 µg mL^{-1}. (b) Fluorescence microscopy images of HaCat cells after 24 h incubation with (A1-2) Nf 12H 0.2R and (B1-2) Nf 12H 0.18R, at concentrations 1: 15 µg mL^{-1} and 2: 25 µg mL^{-1}. (c) Fluorescence microscopy images of HaCat cells after 24 h incubation with (A1-2) Nf@citrate 6H 0.18R, (B1-2) Nf@citrate 12H 0.2R and (C1-2) Nf@citrate 12H 0.18R, at concentrations 1: 15 µg mL^{-1} and 2: 25 µg mL^{-1}.

The results regarding the glioblastoma cells show similar internalization of the Nfs. For both cases, fluorescence is located on the outer lining of the cell and shows possible accumulation of the Nfs at the cell membranes (Fig. 16(a)–(c)). It is important to note that the abovementioned protocols concern qualitive techniques of visualization. The conclusions that can be drawn are suggestions that should be further confirmed by a quantitative technique to ensure scientific plenitude of their biological perspective in theranostics. Thus, quantitative techniques were also used to verify and confirm the abovementioned results.

2.4.4. ROS assay. Knowledge around the mechanism of action of nanoparticles is a key aspect for the design of efficient and safe nanosystems. One of the most known mechanisms of induced toxicity of nanoparticles is the formation of ROS species, which causes oxidative stress to cells and eventually leads to cell death.[46–48] The results of the ROS Assay obtained, show a significant difference between the two cell lines. The fluorescence measured is analogous to the amount of ROS species formed. In the case of HaCat cells it is shown that none of the Nfs cause the formation of ROS species as much as the positive control.(Fig. 17) On the contrary, all the Nfs exceed the amount of ROS species formed compared to the positive control. The abovementioned result confirms the previous results of the biological evaluation and underlines the possible sensitivity of glioblastoma cells towards the synthesized Nfs. The generation of ROS species can be attributed to the composition of the Nfs of iron and silver. The exact mechanism that shows if both or one of the elements are involved in the production of ROS cannot be concluded and further studies are essential to provide such knowledge.[49,50] Despite the lack of the exact mechanism that induces the production of ROS species, the results of the present study are of high importance due to the lack of literature on the discussed Nfs. Nevertheless, individual silver and iron nanoparticles have been thoroughly studied regarding ROS induction. As suggested by literature it is known that silver induces overproduction of ROS by the disruption of balance between oxidants and antioxidants. Accordingly, iron causes the production of ROS by participating in Fenton/Fenton-like reactions that produce oxidative species. One of the most known mechanisms of ROS induction of iron nanoparticles is ferroptosis, which leads evidently to cell death.[51,52] Thus, the ROS production is attributed to both iron and silver. By comparison of the results between the two cell lines, it is noted that ROS production is higher in the case of glioblastoma cells. The abovementioned can be explained based on recent literature that has proved that cancer cells due to higher accumulation of iron cause the increased ROS production that subsequently leads to the initation of ferroptosis in cells.[36–39] Finally, it is important to note that the observation of higher ROS levels in cancer cells compared to healthy cells has been recently reported for hybrid silver–iron nanospikes. The difference between the present and referred study is that the referred study focuses on nanospikes that have iron oxide as center and silver as coating, whereas the present study focuses on nanoflowers with silver as the core and iron oxide as petals. (Fig. 17 and 18).[26]

2.4.5. Limitations. It is imperative to acknowledge the limitations of the results obtained thus far and to emphasize that while their significance is crucial, additional complementary studies are necessary to draw definitive conclusions regarding their anticancer efficacy. For example, investigations into the mechanisms by which iron and silver induce reactive oxygen species (ROS) and the respective contributions of each to the observed toxicity are essential for elucidating the precise mechanism. This is also related to the MTT assay, where examining the specific metabolic pathways leading to cell death can provide valuable insights into the roles of iron and silver, the impact of morphology, and the differences between coated and uncoated nanoflowers. Furthermore, internalization studies could be enhanced through the use of higher-resolution microscopy and specific dyes, such as DAPI, lysotrackers, and mitotrackers, to identify the exact organelles where nanoflowers are localized within cells, thereby enabling meaningful correlations with other data.

2.4.6. Apoptosis–necrosis evaluation. The overall physicochemical profile and biological properties of the Nfs did not exhibit significant differences between different syntheses. Consequently, Nfs 12H 0.2R were selected due to their enhanced permeability, as demonstrated in internalization studies, to evaluate the mechanism of action of the Nfs. This evaluation is of critical importance to determine their further modification to achieve the design and synthesis of selective nanosystems with desired biological properties and to comprehensively understand their interactions with cells. As illustrated in Fig. 19(A) ad (B), Nfs appear to reduce the viability of cancer cells to a greater extent when compared to the respective viability of healthy cells. Furthermore, it is noteworthy that the apoptosis and necrosis results are also higher in the case of glioblastoma cells, when compared to HaCat cells. (Fig. 19) The results suggest that the Nfs exhibit anticancer activity, which is consistent with the rest of the biological evaluation. The abovementioned conclusion of the apoptosis study agrees also with a very similar type of nanoparticles that was recently reported where the nanoparticles were found to induce high toxicity in different cancer cell lines and no significant toxicity in healthy cells.[26]

Finally, it is noteworthy that these Nfs have not, to our knowledge, been extensively studied using these protocols in the existing literature.

2.4.7. Internalization mechanism. As extensively documented in the literature, the precise mechanism of nanoparticle internalization can significantly influence their biological activity, and it is crucial to elucidate this process when designing selective nanosystems for specific biological targets of diseases. The protocol employed facilitates the determination of the internalization pathway through the use of selective inhibitors of metabolic pathways.[53] As shown in Fig. 20(A) for the case of U87-MG cells, the mechanism of internalization involves a combination of pinocytosis and caveolin-mediated endocytosis. The diminutive size of the Nfs elucidates their uptake through caveolin-mediated endocytosis, as their dimensions do not exceed 90 nm.[54] Moreover, the presence of larger Nfs substantiates the observation of pinocytosis, which occurs for particles of greater size.[55]
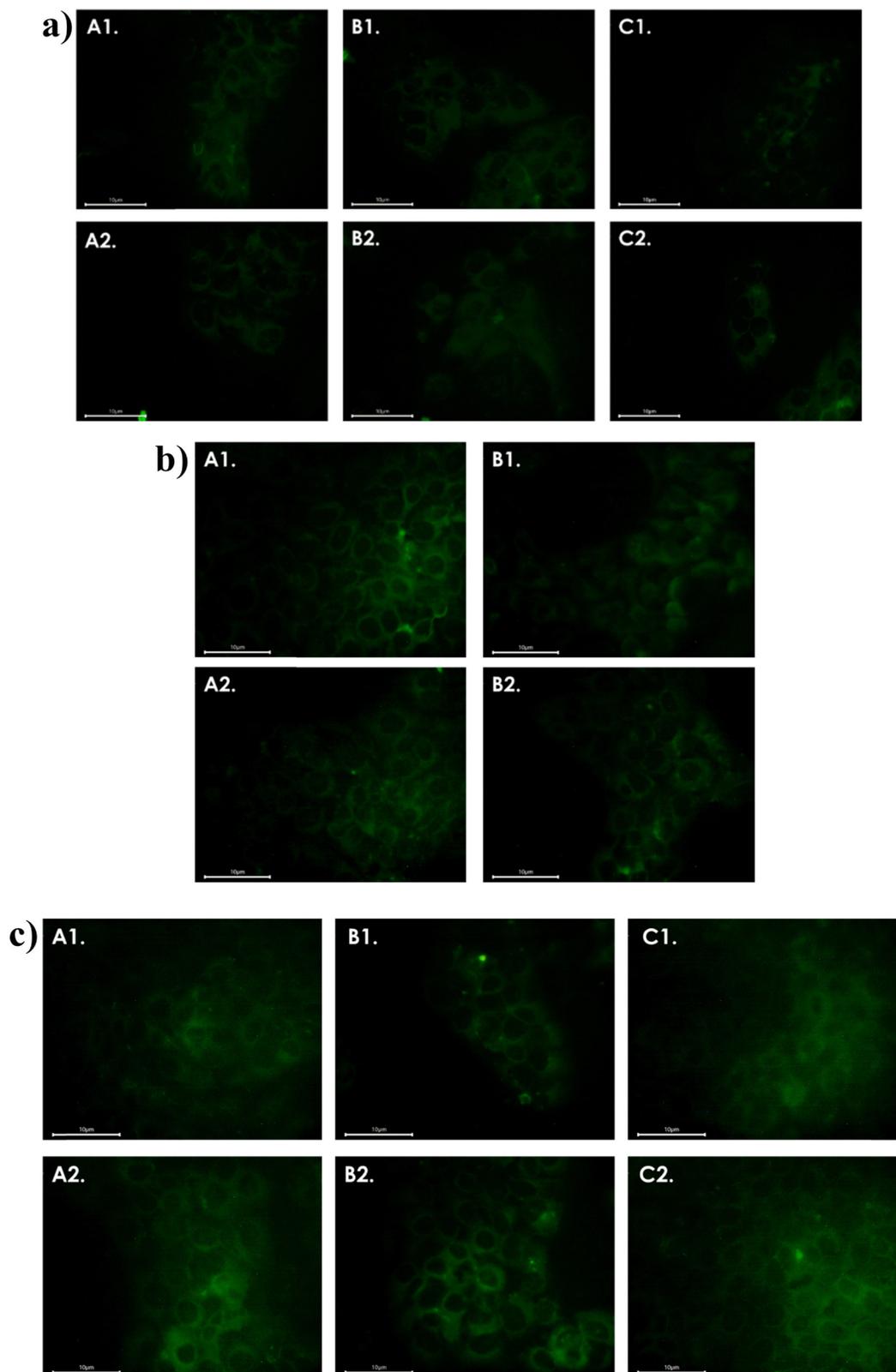
Fig. 16 (a) Fluorescence microscopy images of U87-MG cells after 24 h incubation with (A1-2) Nf 24H 0.2R, (B1-2) Nf 8H 0.15R and (C1-2) Nf 6H 0.18R, at concentrations 1: 15 μg mL^{-1} and 2: 25 μg mL^{-1}. (b) Fluorescence microscopy images of U87-MG cells after 24 h incubation with (A1-2) Nf 12H 0.2R and (B1-2) Nf 12H 0.18R, at concentrations 1: 15 μg mL^{-1} and 2: 25 μg mL^{-1}. (c) Fluorescence microscopy images of U87-MG cells after 24 h incubation with (A1-2) Nf@citrate 6H 0.18R, (B1-2) Nf@citrate 12H 0.2R and (C1-2) Nf@citrate 12H 0.18R, at concentrations 1: 15 μg mL^{-1} and 2: 25 μg mL^{-1}.
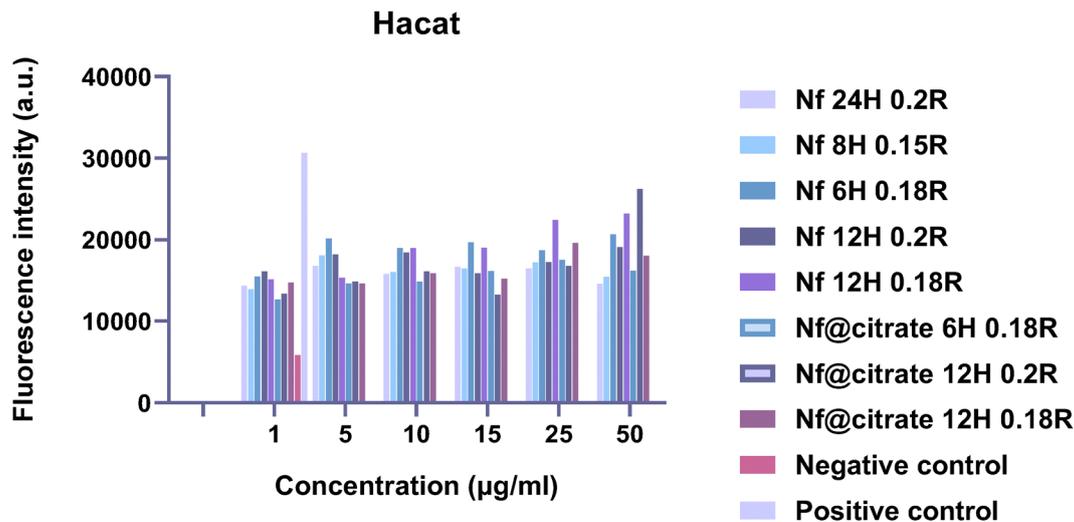
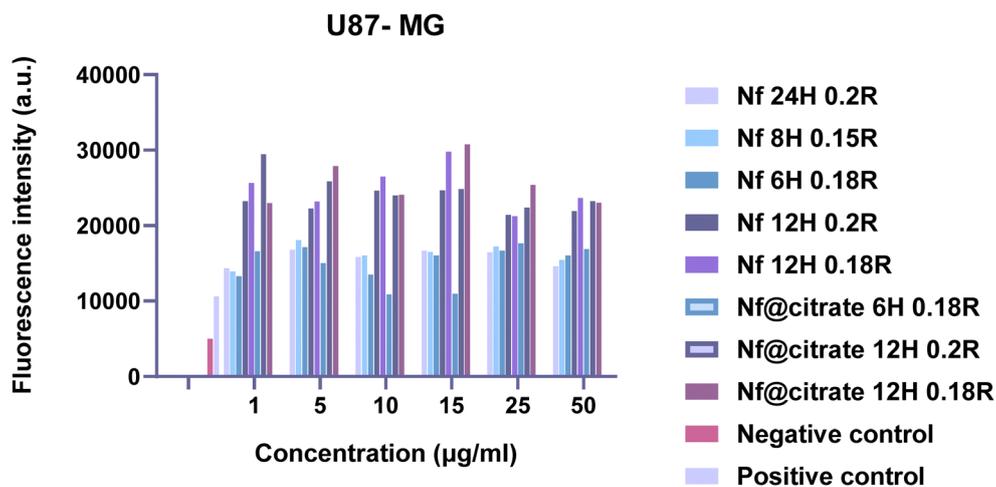**Fig. 17** ROS Assay results of the synthesized Nfs evaluated at healthy cells (HaCat).

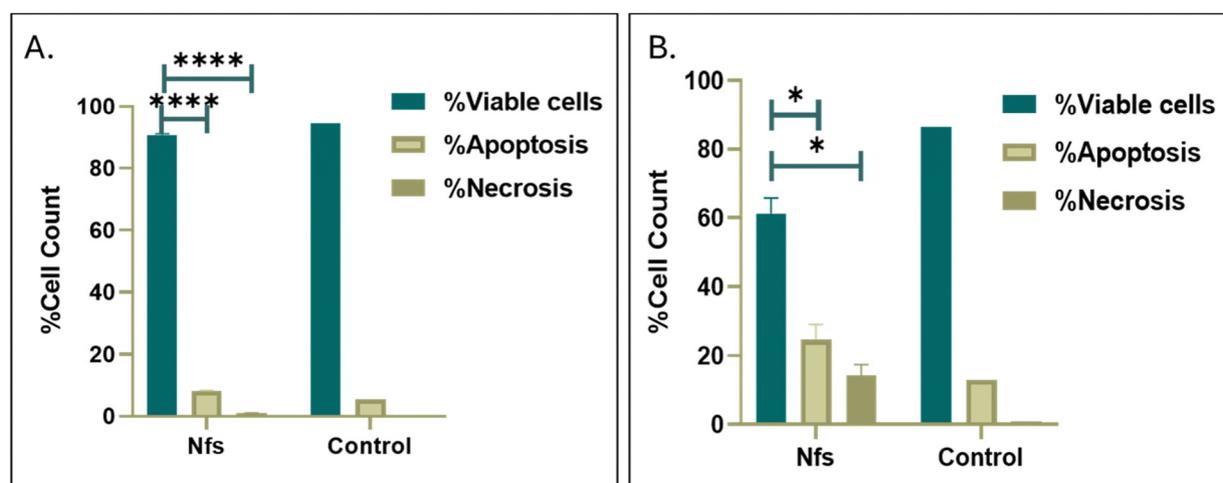**Fig. 18** ROS Assay results of the synthesized Nfs evaluated at U87-MG.

Fig. 19 Apoptosis–necrosis evaluation in: (A) HaCaT and (B) U87-MG after 24 h incubation with NFs.
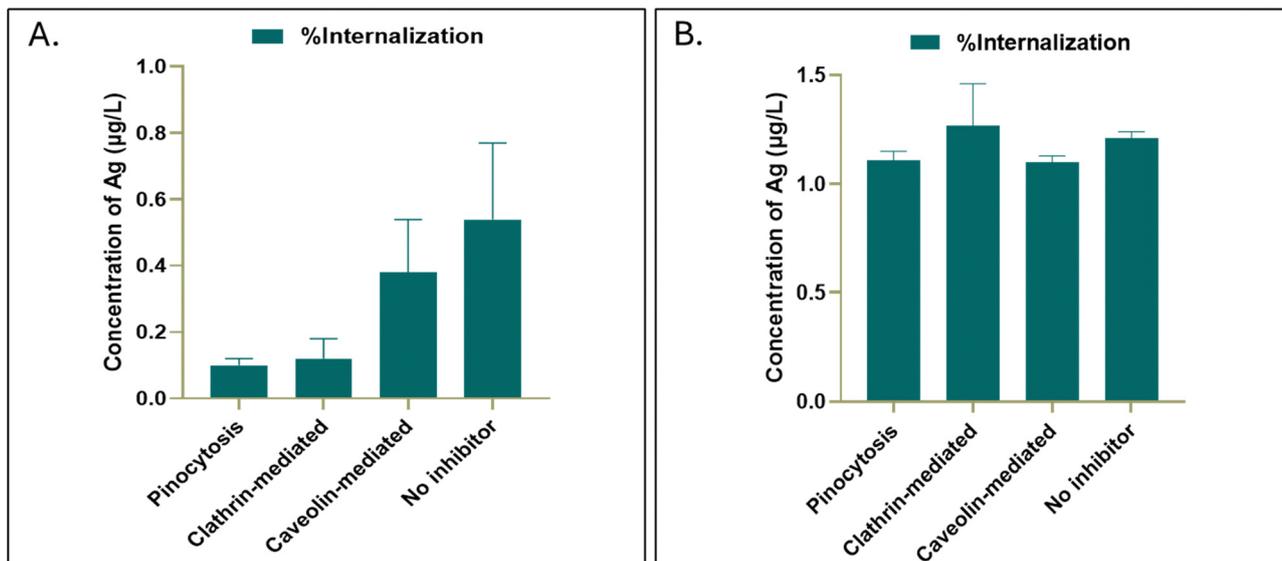
Fig. 20 Incubation of Nfs with inhibitors of specific endocytosis pathways in a (A) HaCat and in (B) U87-MG.

In the case of HaCat cells (Fig. 20(B)), the results indicate the absence of a specific internalization mechanism; rather, the Nfs enter the cells *via* three distinct mechanisms, with pinocytosis being the predominant mode of cellular entry. As previously noted, the larger Nfs enter cells through pinocytosis, while smaller Nfs utilize a combination of clathrin and caveolin-mediated endocytosis. This conclusion has been corroborated in the literature for this particular cell line.[56] The elucidation of the internalization pathway can serve as a foundation for the understanding the processes and steps involved into the observed biological activity of the Nfs.

3. Experimental

3.1 Equipment

Attenuated total reflectance Fourier transform infrared (ATR-FTIR) spectra were obtained on PerkinElmer Spectrum 100 Spectrometer; the spectra were scanned over the range 4000–400 cm^{-1}. Dynamic light scattering (DLS) measurements were performed on a Malvern Instruments Zetasizer Nano Series. In the data presented in this study, each measurement represents the average value of 3 measurements, with 11 to 15 runs for each measurement. Ultraviolet-visible (UV-Vis) absorption spectra in the wavelength range of 200–800 nm was obtained on a Jasco V-650 spectrometer. An ultrasonic bath was used for sonication (Elma Sonic, S 30H).

3.2 Materials and methods

Silver nitrate 99% (AgNO$_3$) was purchased from Fischer, ethylene glycol (EG) 99% and poly-L-lysine 0.01% were purchased from Merck, Polyvinylpyrrolidone (PVP) (M_W = 10 000) were purchased from Alfa Aesar. Iron(III) nitrate·9H$_2$O was purchased from Riedel-de Haen. Trisodium citrate (Citrate Potassium Dihydrogen Phosphate) and sodium acetate anhydrous was purchased from Lach-Ner. Ethanol 99% was purchased from Carlo Erba SA. DMEM high glucose, FBS 10%,

Penicillin–Streptomycin 10%, Glutamine 5% were purchased from Biosera. MTT was purchased from Cayman Chemical Company. Adenine > 99% was purchased from Apollo Scientific. 1,10-Phenanthroline hydrate was purchased from Fluorochem. Eosin was purchased from ROTH.

3.3 Synthesis of silver–iron oxide Nfs (SIONFs)

The synthesized Nfs were prepared according to a solvothermal method with some modifications.[10,17] In a spherical glass vial 10 mL of EG were added followed by the addition of different amounts of Fe(NO$_3$)$_3$·9H$_2$O and stirred until totally dissolved. The synthesis continues by the addition of different amounts of silver nitrate and sodium acetate and the mixture is stirred for at least 30 min, until the solids are completely dissolved. Then, the mixture is transferred into a Teflon lined autoclave reactor and left at 200 °C for different reaction times (6 h, 8 h, 12 h, 24 h). The color of the mixture turns from intense orange into black-brown and the resulting solution was magnetically separated. The resulting precipitate was washed several times with ethanol and water to discard unreacted reagents. Then the precipitate was redispersed in water for further use.

3.4 Physicochemical characterization

The size, morphology, and structural characteristics of the Nfs were determined by a combination of techniques (TEM, DLS, UV-Vis, FT-IR and PXRD). The morphology of the Nfs was confirmed by TEM and their size was estimated. DLS data were also acquired to verify the size of the Nfs as well as their surface charge, which is another important aspect of their characteristics, *via* Zeta Potential measurements. FT-IR spectra and PXRD confirmed the structural characteristics of the Nfs.

3.5 Determination of iron concentration of the Nfs

The concentration of iron in the synthesized Nfs was determined by the colorimetric phenanthroline assay. Iron has the

ability to form stable complexes with 1,10-phenanthroline resulting into strong orange red colored solutions that exhibit high absorbance values in the UV-Vis region and more specifically at 510 nm[57]. The Nfs are digested in HCl (1 : 1) v/v at 70 °C for 30 min. The digested Nfs are diluted with water. Then the following reagents are added to eppendorfs (450 μL sodium acetate 125 mg mL^{-1}, 50 μL hydroxylamine hydrochloride 10 mg mL^{-1}, 200 μL of the sample and 300 μL, 1,10 phenanthroline 10 mg mL^{-1}). Each sample is assessed in triplicates for repeatable results. For the quantification of the iron concentration prior to the samples, the procedure is repeated for known concentrations of iron to create a calibration curve.

3.6 Determination of silver concentration of the Nfs

The amount of silver in the Nfs was quantified by a colorimetric method that is based on the absorbance of the pink complex between silver–adenine and eosin.[58] First, the Nfs were digested with 1 M HNO$_3$ at 50 °C until the solution is clear of color. Then, the Nfs are diluted with water to 1 mL. The following step was the addition of 300 μL of adenine solution 10^{-2} M, 500 μL of PVP 1% aqueous solution, 2.5 mL phosphate buffer pH 6, 500 μL eosin 10^{-3} M. and 595 μL of each sample of the Nfs. The same procedure was followed to create a standard curve using different concentrations of silver, which was used to calculate the amount of silver in the samples.

3.7 Computed tomography imaging

A second generation Mediso microPET/CT scanner (nanoPET/CT, Mediso, Hungary) at the Edinburgh Preclinical Imaging Laboratory was employed to assess the computer tomography (CT) contrast enhancement capabilities of the silver Nfs and silver Nfs coated with citrate. The CT imaging and analysis method has been previously described.[59–61] Imaging parameters included a tube voltage of 50 kVp, 300 ms exposure time, and 0.38 mm slice thickness. Attenuation coefficients were normalized to water, with subsequent conversion of CT image pixels to Hounsfield Units (HU) according to the following equation:

$$ HU = 1000 \frac{\mu - \mu_{water}}{\mu_{water} - \mu_{air}} $$

where μ is the linear attenuation coefficient in each pixel measured by the CT scanner, and μ_{water} and μ_{air} are the linear attenuation coefficients of water and air, respectively. CT images were analyzed using an in-house software.[62,63] A cylindrical volume of interest was drawn at the center of each sample tube (excluding the boundary areas) and were used to quantify the mean HU values and standard deviation.

3.8 Hemocompatibility study

The primary evaluation of the synthesized Nfs' toxicity was performed by use of the hemolysis assay. Clinical discarded blood sample was used for hemolysis assay. The procedure was followed according to existing protocol.[12] First, RBCs were isolated from whole blood by centrifugation at 3000 rpm for 5 min and washed twice with DPBS. The samples of the Nfs were prepared at 15 μg mL^{-1} and 25 μg mL^{-1} concentrations

for a final volume of 300 μL. In 2 mL eppendorfs the following were added in the mentioned order: 285 μL of each sample, 15 μL of RBCs and incubated for 3 h at 37 °C synthesized. For the isolation of the supernatant containing the released hemoglobin, the samples were centrifuged at 3000 rpm for 5 min and 100 μL of the supernatant of each sample were transferred in a 96-well plate. For the isolation of the supernatant containing the released hemoglobin, the samples were centrifuged at 3000 rpm for 5 min and 100 μL of the supernatant of each sample were transferred in a 96-well plate. As positive control was used water that cause full hemolysis of RBCs and releasw of hemoglobin and as negative control was used DPBS without Ca^{2+} and Mg^{2+}. The % Hemolysis was calculated by measuring the plate at 490 nm using an Eliza plate reader and the appropriate equation:

$$ \% \, Hemolysis = \frac{OD_{sample} - OD_{negative\ control}}{OD_{positive\ control} - OD_{negative\ control}} \% $$

where OD_{sample} is the absorbance of the sample, $OD_{positive\ control}$ is the absorbance of the positive control (Water) and $OD_{negative\ control}$ is the absorbance of the negative control (DPBS).

For the completed evaluation of the hemocompatibility profile of the Nfs, the treated RBCs were morphologically evaluated by optical microscopy. In detail, the RBCs were seeded in 24-well plates and incubated for 3 h with the Nfs at the selected concentrations. At the end of the incubation, the RBCs were observed under the optical microscope for the examination of possible structure alterations induced by Nfs' toxicity.

3.9 Cell culture

Cytotoxicity assessment of the synthesized nanoparticles as well as their cellular uptake was performed at two different cell lines: healthy (HaCat, human epidermal keratinocyte healthy cell line) and U87-MG: Uppsala 87 Malignant Glioma cancer cell line. The cells were cultured in a Dulbecco's Modified Eagle Medium high in glucose (DMEM) containing 10% Fetal Bovine Serum (FBS), 10% Penicillin–Streptomycin and 5% Glutamine inside a CO$_2$ incubator (37 °C, 5% CO$_2$).[64]

3.10 *In vitro* cytotoxicity study

The effect on the viability of the cells for the two different cell lines was measured with the MTT assay, according to the established protocol.[65] The method is based on the ability of live cells to reduce MTT (3-(4,5-dimethylthiazol-2-yl)-2,5-Diphenyltetrazolium bromide) *via* their mitochondrial reductase into purple dissoluble formazan crystals. Those crystals are solubilized and based on the intensity of the absorption it is allowed to assess the viability of the cells. Briefly, in a 96-well plate cells were seeded and incubated for 24 h. The culture medium was removed and replaced by the samples in triplicates and different concentrations (50, 25, 15, 10, 5, 1 μg mL^{-1} of iron). After 24 h incubation, the medium was removed, 100 μL of MTT (3-(4,5-dimethylthiazol-2-yl)-2,5-diphenyltetrazolium bromide) (1 mg mL^{-1}) was added to each well and left for 3 h for the formation of the formazan crystals. The formazan crystals were dissolved in DMSO (Dimethyl sulfoxide), and their absorbance was measured at 540 nm (with reference filter at 620 nm) using an Eliza plate reader. The

absorbance values were used for the calculation of the % Viability according to the equation:

$$\%\text{Viability} = \frac{\text{OD(sample)}}{\text{OD(control)}}\%$$

where OD$_{\text{(sample)}}$ is the average absorbance of the sample, OD$_{\text{(Control)}}$ is the average absorbance of the control samples containing only cells. From the measurements of the absorbance standard deviation is calculated for each concentration evaluated.

3.11 Internalization studies

3.11.1 Investigation of internalization by Prussian blue protocol. The visualization of nanoparticle uptake by HaCat or U87-MG cells was achieved by the Prussian Blue staining method. Cells were seeded in 12-well plates at a cell density of 1×10^5 cells per well and incubated for 24 h, until confluent. The culture medium was then removed and replaced by culture medium containing each sample at a concentration of 15 μg mL^{-1} and 25 μg mL^{-1}. After 24 h of incubation, the medium was removed, the cells were washed with PBS and fixated with 4% formalin in PBS for 20 min at 37 °C. The fixated cells were washed twice with PBS, incubated with Pearls solution (1:1 solution of 4% w/v K$_4$Fe (CN)$_6$·3H$_2$O in PBS and 4 M HCl in PBS) for 30 min and washed again with PBS. Neutral red solution (0.02%) was added for 15 min and washed with PBS. The cells were immediately studied with optical microscopy.

3.11.2 Investigation of internalization by fluorescence microscopy. The internalization of the Nfs by HaCat and U87-MG cells was also monitored by fluorescence microscopy. Each cell line was seeded in 0.22 cm^2 coverslips at 10^5–10^6 cell density, into six-well plates. The cells were incubated at 37 °C under CO$_2$ (5%) for 24 h, until confluence of the wells was achieved. The medium was then discarded and replaced by the tested concentrations of the Nfs (15 μg mL^{-1} and 25 μg mL^{-1}) following incubation for 24 h. At the end of the treatment cells were washed three times with PBS, and fixed by using 4% formalin in PBS for 20 min. The cells were washed again three times with PBS and the coverslip was placed on the fluorescence microscope stage for observation.

3.12 ROS assay

To assess oxidative stress induced by the Nfs, the DCFDA assay protocol was employed, with fluorescence measurements obtained using a plate reader. For both cell lines, cells were seeded in 96-well plates and grown to confluence. The culture media was then replaced with selected concentrations of coated and uncoated Nfs and incubated for 24 hours. Following incubation, the supernatant was discarded, and the cells were gently washed with PBS. Subsequently, 100 μL of DCFDA solution was added to each well and incubated in the dark for 30 minutes. For fluorescence intensity comparisons, PBS was used as the negative control, while hydrogen peroxide served as the positive control. Fluorescence intensity was then measured using a fluorescent plate reader.[66–68]

3.13 Apoptosis–necrosis evaluation (FACS, flow cytometry)

Both U87-MG and HaCat cells were seeded in 6 well plates or 25 mm^2 culture flask for 24 h prior to their treatment with 15 μg mL^{-1} of Nfs 12H 0.2R. After 24 h of treatment, cells were harvested by trypsin and then centrifuged at 800 rpm for 3 min. For the Annexin-7AAD protocol, about 1×105 cells were well resuspended in 100 μL of binding buffer, then stained 5 μL of annexin-V and 5 μL of 7AAD and left to incubate for 20 min in the dark. After the incubation time was over, 400 μL of binding buffer was added and the sample was measured with a Becton Dickinson FACS Calibur flow cytometer (BD Bioscience, New Jersey, USA).

3.14 Internalization mechanism

For the identification of the endocytosis pathway of Nfs, cells were seeded into 24-well plates for both cell lines studied until confluency reached 80–90%. The selected inhibitors were then added to the cells (a) Cytochalasin A 10 μg mL^{-1}, (b) Chlorpromazine 10 μg mL^{-1} and (c) Genistein 25 μg mL^{-1} and were incubated for 1 h. The cells were subsequently washed with PBS and the Nfs were added for 24 h incubation at a concentration of 15 μg mL^{-1}. At the end of the incubation time, cells were washed again with PBS, dettached with 200 μL trypsin and collected. Finally, 1 mL of HNO$_3$ 1 M and 1 mL 30% H$_2$O$_2$ were added and samples were left for 2 h at 95 °C. The results were obtained using ICP-MS.

3.15 Statistical analysis

Statistical analyses were conducted utilizing GraphPad Prism as the statistical software. Based on the data input and the null hypothesis, which determines the parameters considered as well as the desired correlations and comparisons to be performed, the appropriate statistical tests were employed. For example, the statistical analysis of the MTT Assay involved the use of one-way ANOVA, which examines the variability of results by considering a single variable and is particularly useful when dealing with three or more groups of data. Conversely, for results corresponding to a single concentration tested but involving different parameters, such as apoptosis–necrosis, the results are suitable for *t*-test statistical analysis. Following this rationale, the statistical analysis was conducted by selecting the most appropriate statistical tool for each experiment implemented.

4. Conclusions

Due to the limited literature on silver–iron oxide nanoflowers, this study provides valuable data supporting their potential use in glioblastoma treatment. By elucidating their synthesis parameters, physicochemical properties, and biological effects, this research enhances the understanding of these hybrid nanosystems, leading to future applications in theranostics and targeted cancer therapies. Recent investigations into the efficacy of hybrid nanoparticles for glioblastoma treatment have yielded promising results, particularly concerning silver–iron hybrid nanoparticles. The dual functionality of these nanoparticles

positions them as ideal candidates for a versatile nanosystem with extensive applications in glioblastoma theranostics. Although morphologies such as nanoflowers have not been extensively documented, a limited number of studies have provided insights into their efficacy as photothermal therapy (PTT) agents. Furthermore, hybrid silver–iron nanoparticles have demonstrated suitability as thermo- and photo-sensitizers in glioblastoma cell testing.[16,69–71]

The synthetic procedure of this study exploits the parameters affecting the development of hybrid silver – iron oxide Nfs and further demonstrates their successful coating with trisodium citrate. Critical parameters of this study including the reaction time and ratio of Ag/Fe demonstrate the impact on the size and formed flower shape of the Nfs. Furthermore, Nfs are characterized as far as their physicochemical properties are concerned, while also evaluated as potential multi-sensitive agents for the theranostic of glioblastoma. The *in vitro* biological evaluation suggests possible anticancer properties and high hemocompatibility, which are essential for the design and synthesis of an efficient and safe nanosystems. Their dual nature leads to their easy tracking by using different methods based on either silver or iron. The results of the CT measurements show that the Nfs are eligible nanosystems for diagnostic purposes, such CT contrast agents. Furthermore, the apoptosis–necrosis evaluation confirmed the hypothesis of the possible anticancer activity of the Nfs in glioblastoma, since the %apoptosis and %necrosis were significantly higher than the respective results of healthy cells. Lastly, the careful examination of the internalization of the Nfs offered a foundation for the detailed explanation and verification of their mechanism of action when interacting with both healthy and cancerous cells. Due to the limited literature data on the current Nfs it is notable to contribute to the literature with more data that support the possible use of these Nfs for biological applications.

Data availability

We submit a manuscript entitled:"Hybrid Silver–Iron Oxide Nanoflowers: Tailoring Morphology and Unlocking Theranostic Potential for Glioblastoma" authored by Sofia G. Nikolopouloua, Beata Kalska-Szostko, Anna Basa, Giorgos Papanastasiou, Adriana Tavares, Carlos Alcaide Corral, Marios Kostakis, Nikolaos S. Thomaidis, Athina Papadopoulou, Eleni K. Efthimiadou. The data supporting this article are available in case requested from the editorial team.

Conflicts of interest

There are no conflicts to declare.

References

1 L. Rong, N. Li and Z. Zhang, Emerging therapies for glioblastoma: current state and future directions, *J. Exp. Clin. Cancer Res.*, 2022, **41**(1), 1–18.

2 R. S. Angom, N. M. R. Nakka and S. Bhattacharya, Advances in Glioblastoma Therapy: An Update on Current Approaches, *Brain Sci.*, 2023, **13**(11), 1536, DOI: 10.3390/brainsci13111536.

3 J. Zhang, M. F. G. Stevens and T. D. Bradshaw, Temozolomide: Mechanisms of Action, Repair and Resistance, *Curr. Mol. Pharmacol.*, 2012, **5**(1), 102–114.

4 M. T. C. Poon, C. L. M. Sudlow, J. D. Figueroa and P. M. Brennan, Longer-term (≥2 years) survival in patients with glioblastoma in population-based studies pre- and post-2005: a systematic review and meta-analysis, *Sci. Rep.*, 2020, **10**(1), 1–10, DOI: 10.1038/s41598-020-68011-4.

5 A. Barzegar Behrooz, Z. Talaie and A. Syahir, Nanotechnology-Based Combinatorial Anti-Glioblastoma Therapies: Moving from Terminal to Treatable, *Pharmaceutics*, 2022, **14**(8), 1–23.

6 S. Ajith, F. Almomani, A. Elhissi and G. A. Husseini, Nanoparticle-based materials in anticancer drug delivery: Current and future prospects, *Heliyon*, 2023, **9**(11), e21227, DOI: 10.1016/j.heliyon.2023.e21227.

7 F. Rodr, P. Caruana, N. Fuente De, P. Español and J. Balart, Nano-Based Approved Pharmaceuticals for Cancer Treatment: Present and Future Challenges, *Biomolecules.*, 2022, **12**(784), 1–27.

8 N. Ebrahimi, S. Rasoul-Amini, A. Niazi, N. Erfani, A. Moghadam and A. G. Y. Ebrahiminezhad, Cytotoxic and Apoptotic Effects of Three Types of Silver-Iron Oxide Binary Hybrid Nanoparticles, *Curr. Pharm. Biotechnol.*, 2016, **17**(12), 1049–1057.

9 A. A. Hernández-Hernández, G. Aguirre-Álvarez, R. Cariño-Cortés, L. H. Mendoza-Huizar and R. Jiménez-Alvarado, Iron oxide nanoparticles: synthesis, functionalization, and applications in diagnosis and treatment of cancer, *Chem. Pap.*, 2020, **74**(11), 3809–3824, DOI: 10.1007/s11696-020-01229-8.

10 R. Das, N. Rinaldi-Montes, J. Alonso, Z. Amghouz, E. Garaio and J. A. García, *et al.*, Boosted Hyperthermia Therapy by Combined AC Magnetic and Photothermal Exposures in Ag/Fe₃O₄ Nanoflowers, *ACS Appl. Mater. Interfaces*, 2016, **8**(38), 25162–25169.

11 Ö. Erdoğan, M. Abbak, G. M. Demirbolat, S. Aksel, S. Paşa and G. Dönmez Yalçin, *et al.*, Treatment of glioblastoma by photodynamic therapy with the aid of synthesized silver nanoparticles by green chemistry from citrus aurantium, *J. Res. Pharm.*, 2021, **25**(5), 641–652.

12 S. G. Nikolopoulou, B. Kalska, A. Basa, A. Papadopoulou and E. K. Efthimiadou, Novel Hybrid Silver – Silica Nanoparticles Synthesized by Modifications of the Sol – Gel Method and Their Theranostic Potential in Cancer, *ACS Appl. Bio Mater.*, 2023, **6**(12), 5125–5874.

13 Y. Zhang, K. Xi, X. Fu, H. Sun, H. Wang and D. Yu, *et al.*, Versatile metal-phenolic network nanoparticles for multi-targeted combination therapy and magnetic resonance tracing in glioblastoma, *Biomaterials*, 2021, **278**, 121163, DOI: 10.1016/j.biomaterials.2021.121163.

14 N. Arias-Ramos, L. E. Ibarra, M. Serrano-Torres, B. Yagüe, M. D. Caverzán and C. A. Chesta, *et al.*, Iron oxide incorporated conjugated polymer nanoparticles for simultaneous use in magnetic resonance and fluorescent imaging of brain tumors, *Pharmaceutics*, 2021, **13**(8), 1258, DOI: 10.3390/pharmaceutics13081258.

15 A. ur Rehman, Y. Wu, H. D. N. Tran, K. Vazquez-Prada, Y. Liu and H. Adelnia, et al., Silver/Iron Oxide Nano-Popcorns for Imaging and Therapy, ACS Appl. Nano Mater., 2021, 4(10), 10136–10147.

16 T. Grancharova, P. Zagorchev and B. Pilicheva, Iron Oxide Nanoparticles: Parameters for Optimized Photoconversion Efficiency in Synergistic Cancer Treatment, J. Funct. Biomater., 2024, 15(8), 207, DOI: 10.3390/jfb15080207.

17 Y. Zhang, H. Ding, Y. Liu, S. Pan, Y. Luo and G. Li, Facile one-step synthesis of plasmonic/magnetic core/shell nanostructures and their multifunctionality, J. Mater. Chem., 2012, 22(21), 10779–10786.

18 T. Analysis, M. J. Jee, J. A. Tyson, E. Glikman and M. Bogosavljevi A comparison of TEM and DLS methods to characterize size distribution of ceramic nanoparticles A comparison of TEM and DLS methods to characterize size distribution of ceramic nanoparticles.

19 S. G. Nikolopoulou, N. Boukos, E. Sakellis and E. K. Efthimiadou, Synthesis of biocompatible silver nanoparticles by a modified polyol method for theranostic applications: Studies on red blood cells, internalization ability and antibacterial activity, J. Inorg. Biochem., 2020, 211, 111177, DOI: 10.1016/j.jinorgbio.2020.111177.

20 S. G. Nikolopoulou, B. Kalska, A. Basa, A. Papadopoulou and E. K. Efthimiadou, Novel Hybrid Silver-Silica Nanoparticles Synthesized by Modifications of the Sol–Gel Method and Their Theranostic Potential in Cancer, ACS Appl. Bio Mater., 2023, 6(12), 5235–5251.

21 A. L. P. Cruz, J. A. G. Cervantes, X. G. V. Anzaldo and G. G. Rivas, Synthesis and design of Ag – Fe bimetallic nanoparticles as antimicrobial synergistic combination therapies against clinically relevant pathogens, Sci. Rep., 2021, 1–11, DOI: 10.1038/s41598-021-84768-8.

22 M. H. Ali, M. A. K. Azad, K. A. Khan, M. O. Rahman, U. Chakma and A. Kumer, Analysis of Crystallographic Structures and Properties of Silver Nanoparticles Synthesized Using PKL Extract and Nanoscale Characterization Techniques, ACS Omega, 2023, 8(31), 28133–28142.

23 K. Srinivas and D. Press, A quality by design approach on polymeric nanocarrier delivery of gefitinib: formulation, in vitro, and in vivo characterization A quality by design approach on polymeric nanocarrier delivery of gefitinib: formulation, in vitro, and in vivo characte, Int. J. Nanomed., 2017, 12, 15–28, DOI: 10.2147/IJN.S122729.

24 M. Danaei, M. Dehghankhold, S. Ataei, F. H. Davarani, R. Javanmard and A. Dokhani, et al., Impact of Particle Size and Polydispersity Index on the Clinical Applications of Lipidic Nanocarrier Systems, Pharmaceutics, 2018, 10(57), 1–17.

25 M. Wang, Y. Liang, Z. Zhang, G. Ren, Y. Liu and S. Wu, et al., Ag@Fe$_3$O$_4$@C nanoparticles for multi-modal imaging-guided chemo-photothermal synergistic targeting for cancer therapy, Anal. Chim. Acta, 2019, 1086, 122–132, DOI: 10.1016/j.aca.2019.08.035.

26 S. S. Moonshi, K. X. Vazquez-Prada, J. Tang, N. J. Westra van Holthe, G. Cowin and Y. Wu, et al., Spiky Silver-Iron Oxide Nanohybrid for Effective Dual-Imaging and Synergistic

27 S. Yedgar and G. Barshtein, Hemolytic Activity of Nanoparticles as a Marker of Their Hemocompatibility, Micromachines, 2022, 13, 2091.

28 S. Malehmir, M. A. Esmaili, M. K. Mahabady, A. Sobhaninasab, A. Atapour and M. R. Ganjali, et al., A review: hemocompatibility of magnetic nanoparticles and their regenerative medicine, cancer therapy, drug delivery, and bioimaging applications, Front. Chem., 2023, 11, 1–14.

29 K. de la Harpe, P. Kondiah, Y. Choonara, T. Marimuthu, L. du Toit and V. Pillay, The Hemocompatibility of Nanoparticles: A Review of Cell–Nanoparticle Interactions and Hemostasis, Cells, 2019, 8(10), 1209.

30 D. Hernández-Moreno, M. Fernández-Díaz, I. Rucandio, J. M. Navas and M. L. Fernández-Cruz, Toxic Effects of Different Coating-Related Functionalized Nanoparticles on Aquatic Organisms, Toxics, 2024, 12(2), 142, DOI: 10.3390/toxics12020142.

31 I. Kim, B. T. Lee, H. A. Kim, K. W. Kim, S. D. Kim and Y. S. Hwang, Citrate coated silver nanoparticles change heavy metal toxicities and bioaccumulation of Daphnia magna, Chemosphere, 2016, 143, 99–105, DOI: 10.1016/j.chemosphere.2015.06.046.

32 J. K. Fard, S. Jafari and M. A. Eghbal, A review of molecular mechanisms involved in toxicity of nanoparticles, Adv. Pharm. Bull., 2015, 5(4), 447–454, DOI: 10.15171/apb.2015.061.

33 C. Nieves Lira, A. P. Carpenter, J. E. Baio, B. J. Harper, S. L. Harper and M. R. Mackiewicz, Size- and Shape-Dependent Interactions of Lipid-Coated Silver Nanoparticles: An Improved Mechanistic Understanding through Model Cell Membranes and In Vivo Toxicity, Chem. Res. Toxicol., 2024, 37(6), 968–980.

34 E. Mansouri, A. Mesbahi, H. Hamishehkar, S. Montazersaheb, V. Hosseini and S. Rajabpour, The effect of nanoparticle coating on biological, chemical and biophysical parameters influencing radiosensitization in nanoparticle-aided radiation therapy, BMC Chem., 2023, 17(1), 1–14, DOI: 10.1186/s13065-023-01099-7.

35 L. Khalef, R. Lydia, K. Filicia and B. Moussa, Cell viability and cytotoxicity assays: Biochemical elements and cellular compartments, Cell Biochem. Funct., 2024, 42(3), e4007, DOI: 10.1002/cbf.4007.

36 C. Hacioglu and F. Kar, Capsaicin induces redox imbalance and ferroptosis through ACSL4/GPx4 signaling pathways in U87-MG and U251 glioblastoma cells, Metab. Brain Dis., 2023, 38(2), 393–408, DOI: 10.1007/s11011-022-00983-w.

37 J. Shi, N. Yang, M. Han and C. Qiu, Emerging roles of ferroptosis in glioma, Front. Oncol., 2022, 12, 1–17.

38 K. Zhu, Y. Cai, L. Lan and N. Luo, Tumor Metabolic Reprogramming and Ferroptosis: The Impact of Glucose, Protein, and Lipid Metabolism, Int. J. Mol. Sci., 2024, 25(24), 1–23.

39 Y. Luo, G. Tian, X. Fang, S. Bai, G. Yuan and Y. Pan, Ferroptosis and Its Potential Role in Glioma: From Molecular Mechanisms to Therapeutic Opportunities, Antioxidants, 2022, 11(11), 2123, DOI: 10.3390/antiox11112123.

40 E. A. Salvanou, A. Kolokithas-Ntoukas, D. Prokopiou, M. Theodosiou, E. Efthimiadou, P. Koźmiński, S. Xanthopoulos,

Thermo-Chemotherapy, ACS Appl. Mater. Interfaces, 2023, 15(36), 42153–42169.

K. Avgoustakis and P. Bouziotis, ^{177}Lu-Labeled Iron Oxide Nanoparticles Functionalized with Doxorubicin and Bevacizumab as Nanobrachytherapy Agents against Breast Cancer, *Molecules*, 2024, **29**(5), 1030, DOI: **10.3390/molecules29051030**.

41 E. D. Prokopiou, M. Pissas, G. Fibbi, F. Margheri, B. Kalska-Szostko, G. Papanastasiou, M. Jansen, J. Wang, A. Laurenzana and K. E. Efthimiadou, Toxicology *in Vitro* Synthesis and characterization of modified magnetic nanoparticles as theranostic agents: *in vitro* safety assessment in healthy cells, *Toxicol. In Vitro*, 2021, **72**, 105094, DOI: **10.1016/j.tiv.2021.105094**.

42 E. Science, Magnetite in the human body: Biogenic *vs.* anthropogenic, *Proc. Natl. Acad. Sci. U. S. A.*, 2016, **113**(39), 11986–11987.

43 A. Girigoswami, B. Deepika, S. Udayakumar, G. Janani, D. J. Mercy and K. Girigoswami, Peony-shaped zinc oxide nanoflower synthesized via hydrothermal route exhibits promising anticancer and anti-amyloid activity, *BMC Pharmacol. Toxicol.*, 2024, **25**(1), 101, DOI: **10.1186/s40360-024-00830-x**.

44 L. Huang, X. Mao, J. Li, Q. Li, J. Shen and M. Liu, *et al.*, Nanoparticle Spikes Enhance Cellular Uptake via Regulating Myosin IIA Recruitment, *ACS Nano*, 2023, **17**(10), 9155–9166.

45 W. Sun, H. Xiao, J. Zhu, Z. Hao, J. Sun and D. Wang, *et al.*, Multifunctional Oxygen-Generating Nanoflowers for Enhanced Tumor Therapy, *ACS Appl. Bio Mater.*, 2023, **6**(11), 4998–5008.

46 Y. Li, J. Yang and X. Sun, Reactive Oxygen Species-Based Nanomaterials for Cancer Therapy, *Front. Chem.*, 2021, **9**, 1–12.

47 A. A. Dayem, M. K. Hossain, S. B. Lee, K. Kim, S. K. Saha and G. Yang, *et al.*, The Role of Reactive Oxygen Species (ROS) in the Biological Activities of Metallic Nanoparticles, *Int. J. Mol. Sci.*, 2017, **18**(120), 1–21.

48 Z. Yu, Q. Li, J. Wang, Y. Yu, Y. Wang, Q. Zhou and P. Li, Reactive Oxygen Species-Related Nanoparticle Toxicity in the Biomedical Field, *Nanoscale Res. Lett.*, 2020, **15**(1), 115, DOI: **10.1186/s11671-020-03344-7**.

49 H. Wu, J. Yin, W. G. Wamer, M. Zeng and Y. M. Lo, Reactive oxygen species-related activities of nano-iron metal and nano-iron oxides 5, *J. Food Drug Anal.*, 2014, **22**(1), 86–94, DOI: **10.1016/j.jfda.2014.01.007**.

50 B. Lee, S. J. Yun and I. Choi, Silver nanoparticles induce reactive oxygen species-mediated cell cycle delay and synergistic cytotoxicity with 3-bromopyruvate in Candida albicans, but not in Saccharomyces cerevisiae, *Int. J. Nanomed.*, 2019, **14**, 4801–4816.

51 J. He, Y. Ma, X. Niu, J. Pei, R. Yan and F. Xu, *et al.*, Silver nanoparticles induce endothelial cytotoxicity through ROS-mediated mitochondria-lysosome damage and autophagy perturbation: The protective role of N-acetylcysteine, *Toxicology*, 2024, **502**, 153734, DOI: **10.1016/j.tox.2024.153734**.

52 Z. Zhao, Iron and oxidizing species in oxidative stress and Alzheimer's disease, *Aging Med.*, 2019, **2**(2), 82–87.

53 G. J. Doherty and H. T. McMahon, Mechanisms of endocytosis, *Annu. Rev. Biochem.*, 2009, **78**, 857–902.

54 W. Zhang, R. Taheri-Ledari, F. Ganjali, S. S. Mirmohammadi, F. S. Qazi and M. Saeidirad, *et al.*, Effects of morphology and size of nanoscale drug carriers on cellular uptake and internalization process: a review, *RSC Adv.*, 2022, **13**(1), 80–114.

55 M. Sousa De Almeida, E. Susnik, B. Drasler, P. Taladriz-Blanco, A. Petri-Fink and B. Rothen-Rutishauser, Understanding nanoparticle endocytosis to improve targeting strategies in nanomedicine, *Chem. Soc. Rev.*, 2021, **50**(9), 5397–5434.

56 V. Laniosz, S. A. Dabydeen, M. A. Havens and P. I. Meneses, Human Papillomavirus Type 16 Infection of Human Keratinocytes Requires Clathrin and Caveolin-1 and Is Brefeldin A Sensitive, *J. Virol.*, 2009, **83**(16), 8221–8232.

57 L. G. Saywell and B. B. Cunningham, Determination of Iron: Colorimetric o-Phenanthroline Method, *Ind. Eng. Chem., Anal. Ed.*, 1937, **9**(2), 67–69.

58 Y. Fujita, I. Mori, M. Toyoda and T. Matsuo, Determination of Silver(I) by an Association Complex Formation between Silver-Adenine and Eosin, *Anal. Sci.*, 1993, **9**(6), 829–834.

59 A. P. Stavropoulou, M. Theodosiou, E. Sakellis, N. Boukos, G. Papanastasiou and C. Wang, *et al.*, Bimetallic gold-platinum nanoparticles as a drug delivery system coated with a new drug to target glioblastoma, *Colloids Surf., B*, 2022, **214**, 112463, DOI: **10.1016/j.colsurfb.2022.112463**.

60 E. D. Prokopiou, M. Pissas, G. Fibbi, F. Margheri, B. Kalska-Szostko and G. Papanastasiou, *et al.*, Synthesis and characterization of modified magnetic nanoparticles as theranostic agents: *in vitro* safety assessment in healthy cells, *Toxicol Vitr*, 2021, **72**, 105094. Available from:.

61 J. Kuhn, G. Papanastasiou, C. W. Tai, C. M. Moran, M. A. Jansen and A. A. S. Tavares, *et al.*, Tri-modal imaging of gold-dotted magnetic nanoparticles for magnetic resonance imaging, computed tomography and intravascular ultrasound: An *in vitro* study, *Nanomedicine*, 2020, **15**(25), 2433–2445.

62 G. Papanastasiou, M. A. Rodrigues, C. Wang, K. Heurling, C. Lucatelli and R. A. S. Salman, *et al.*, Pharmacokinetic modelling for the simultaneous assessment of perfusion and 18F-flutemetamol uptake in cerebral amyloid angiopathy using a reduced PET-MR acquisition time: Proof of concept, *Neuroimage*, 2021, **225**, 117482, DOI: **10.1016/j.neuroimage.2020.117482**.

63 B. Bier, M. Unberath, T. Geimer, J. Maier, G. Gold and M. Levenston, *et al.*, Motion compensation using range imaging in C-arm cone-beam CT, *Communications in Computer and Information Science*, 2017, vol. 723, pp. 561–570.

64 K. Phelan and K. M. May, *Mammalian Cell Tissue Culture Techniques*. 2016, pp. 1–23.

65 P. Kumar, A. Nagarajan and P. D. Uchil, Analysis of cell viability by the MTT assay, *Cold Spring Harb. Protoc.*, 2018, **2018**(6), 469–471.

66 J. Zhao and M. Riediker, Detecting the oxidative reactivity of nanoparticles: a new protocol for reducing artifacts, *J. Nanoparticles Res.*, 2014, **16**(7), 2493, DOI: **10.1007/s11051-014-2493-0**.

67 M. P. Murphy, H. Bayir, V. Belousov, C. J. Chang, K. J. A. Davies and M. J. Davies, *et al.*, Guidelines for measuring reactive oxxygen species and oxidative damage in cells and *in vivo*, *Nat. Metab.*, 2022, **4**, 651–662.

68 C. P. Rubio and J. J. Cerón, Spectrophotometric assays for evaluation of Reactive Oxygen Species (ROS) in serum: general concepts and applications in dogs and humans, *BMC Vet. Res.*, 2021, **8**, 1–13.

69 V. Manescu, I. Antoniac, G. Paltanea, I. V. Nemoianu, A.G. Mohan and A. Antoniac, *et al.*, Magnetic Hyperthermia in Glioblastoma Multiforme Treatment, *Int. J. Mol. Sci.*, 2024, **25**(18), 10065, DOI: **10.3390/ijms251810065**.

70 A. Spoială, C. I. Ilie, L. Motelica, D. Ficai, A. Semenescu and O. C. Oprea, *et al.*, Smart Magnetic Drug Delivery Systems for the Treatment of Cancer, *Nanomaterials*, 2023, **13**(5), 876, DOI: **10.3390/nano13050876**.

71 A. Van de Walle, A. Figuerola, A. Espinosa, A. Abou-Hassan, M. Estrader and C. Wilhelm, Emergence of magnetic nanoparticles in photothermal and ferroptotic therapies, *Mater. Horiz.*, 2023, **10**(11), 4757–4775.